The geochemical signatures of the Silurian–Devonian succession in eastern Saudi Arabia

Mohamed SOUA[ID]

Department of Geological Operations, Saudi Aramco, Dhahran, Saudi Arabia

Abstract: This study was performed on 663 sandstone core and cutting samples taken from the Silurian–Devonian succession in five wells, located in eastern Saudi Arabia. This study aimed to correlate the Tawil Formation in the study wells, defining the lower Qalibah/Tawil and upper Tawil/Jauf boundaries. The Tawil Formation is mostly characterized by clastic-dominated fluvial to marginal marine depositional environments.

A chemostratigraphic correlation workflow was established using key element ratios and comprising four zones (C1 to C4) and five subzones (C2-1 to C2-3 and C3-1-C3-2).

The chemostratigraphic zonation allowed robust characterization of stratigraphy in the uppermost Qalibah, Tawil, and lower Jauf Formations. Zone C1 is associated in most cases with the Sharawra Formation. Zones C2 and C3 are generally linked with the Tawil Formation, and Zone C4 broadly defines the lower part of Jauf Formation. In detail, the chemostratigraphic zonal boundaries do not precisely match the biostratigraphical and lithostratigraphic boundaries, indicating that the C1-C2 and C3-C4 boundaries are probably time-transgressive.

The ratio Zr/Nb was used to model sequence stratigraphy. This ratio can vary in proportion to grain size, in which the element Zr is known to be concentrated in the heavy mineral zircon; while Nb-bearing heavy minerals along with clay minerals, likely illite, produce Nb. The increasing Zr/Nb ratio values are considered to define the coarsening upward or regressive sequences while decreasing Zr/Nb trends can mark fining upward or transgressive sequences.

Key words: Tawil Formation, chemostratigraphy, clastic sediments, sequence stratigraphy

1. Introduction

1.1. Background on the Silurian–Devonian

During the late Silurian–Early Devonian, the Tawil Formation developed on a stable Paleozoic epicontinental area; its distribution was controlled by the paleotopography ramp setting. It is characterized as a clastic-dominated depositional environment, which varies from fluvial to marginal marine conditions, in an overall progradational sequence. This reflects the beginning of a new transgressive cycle during the Devonian (Steineke et al., 1958; Powers et al., 1966; Janjou et al., 1997; Rahmani et al., 2002; Laboun, 2010). In general, it is equivalent to the Arabian TMS AP3 mega-sequence of Sharland et al. (2001).

The purpose of this paper is to evaluate the Silurian–Devonian section including Sharawra, Tawil, and Jauf Formations from a chemostratigraphic point of view using core and cutting samples to develop a regional correlation for the wells encountered in eastern Saudi Arabia, since biostratigraphy does not provide a high level of resolution in most of the study wells.

1.2. Geological setting

The study wells (Figure 1) include the upper Qalibah, Tawil, and lower Jauf Formations. According to Wender et al. (1998), the Tawil sandstones are more compacted and silica-cemented with parts bearing kaolinite, which makes it distinctive from the overlying Jauf Formation. The lowermost section of the Jauf Formation, the Shaiba Member, is characterized by alternation of transgressive shaly and sandy sediments with thin carbonate beds, in the Northwestern part of Saudi Arabia. In eastern areas, Rahmani et al. (2002) described it as a progradational sequence. The contact between the Jauf and Tawil was considered conformable (e.g., Powers, 1968; Al-Hajri et al., 1999), but the absence of the Juraniyat Member (the upper most Tawil) in some areas indicates an unconformable contact (Wallace et al., 1996; Steemans et al., 2007).

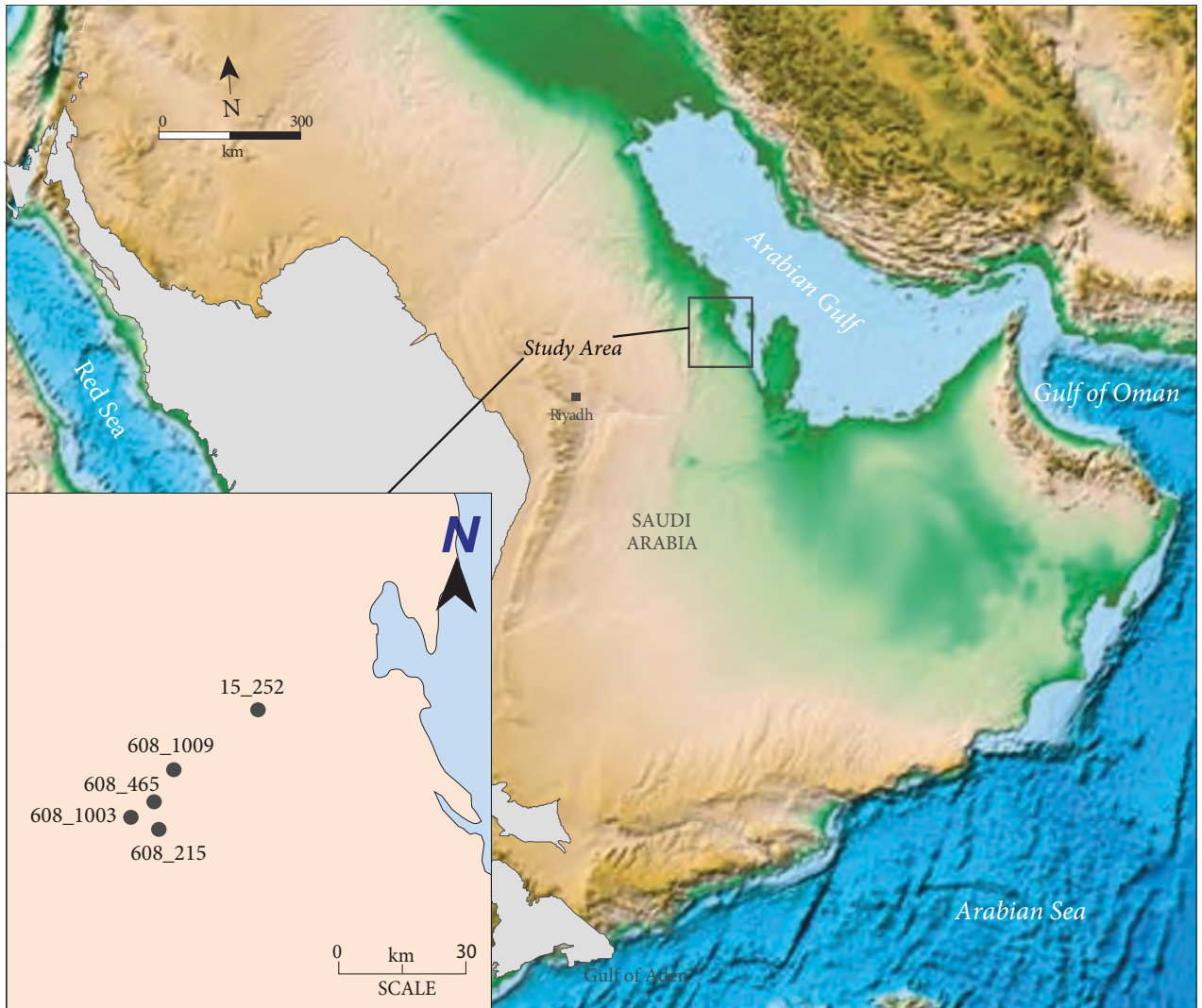* Correspondence: mohamed.soua@aramco.com

Figure 1. Location map displaying the location of the studied wells.

The lower part of the Tawil Formation is generally characterized by shallow marine sediment succeeded by fluvial to continental clastics (Sharland et al., 2001).

The boundary between the underlying Sharawra and the Tawil Formations is characterized by an unconformity pertaining to the Ludlow Stage of the Late Silurian. The Silurian–Devonian clastic succession gently dips westward; the base is defined at the pre-Tawil Unconformity (PTU) and the top by the base of the overlying Shaiba Member (Figure 2) (e.g., Wender et al., 1998; Al-Ramadan et al., 2004). Three depositional cycles for the Silurian–Devonian succession have been defined by Laboun (2010): the pre-Acadian (Qusaiba and Sharawra Formations), the syn-Acadian (Tawil Formation) and the post-Acadian (Jauf Formation). According to Laboun (2010), the PTU defines the boundary between Tawil Formation and underlying units (Silurian to Late Ordovician, Sharawra, Qusaiba, and Sarah Formations), and is associated with the Acadian tectonic movement.

The Tawil Formation is considered by Wender et al. (1998) and Al-Ramadan et al. (2004) to be dominated by sandstones and shales deposited within fluvial to marginal marine environment. According to Al-Hajri et al. (1999), the Jauf Formation is deposited over a broad shelf and channel sandstones, while Rahmani et al. (2002) suggested orbitally-forced coastal plain/deltaic environment of deposition.

Biostratigraphic analysis of the Tawil Formation in the subsurface has been based mainly on palynology (e.g., Stump et al., 1995; Al-Hajri and Paris, 1998; Al-Hajri et al., 1999; Dossary et al., 2017), but it is unfortunate that some of the Tawil section was barren in the study wells,
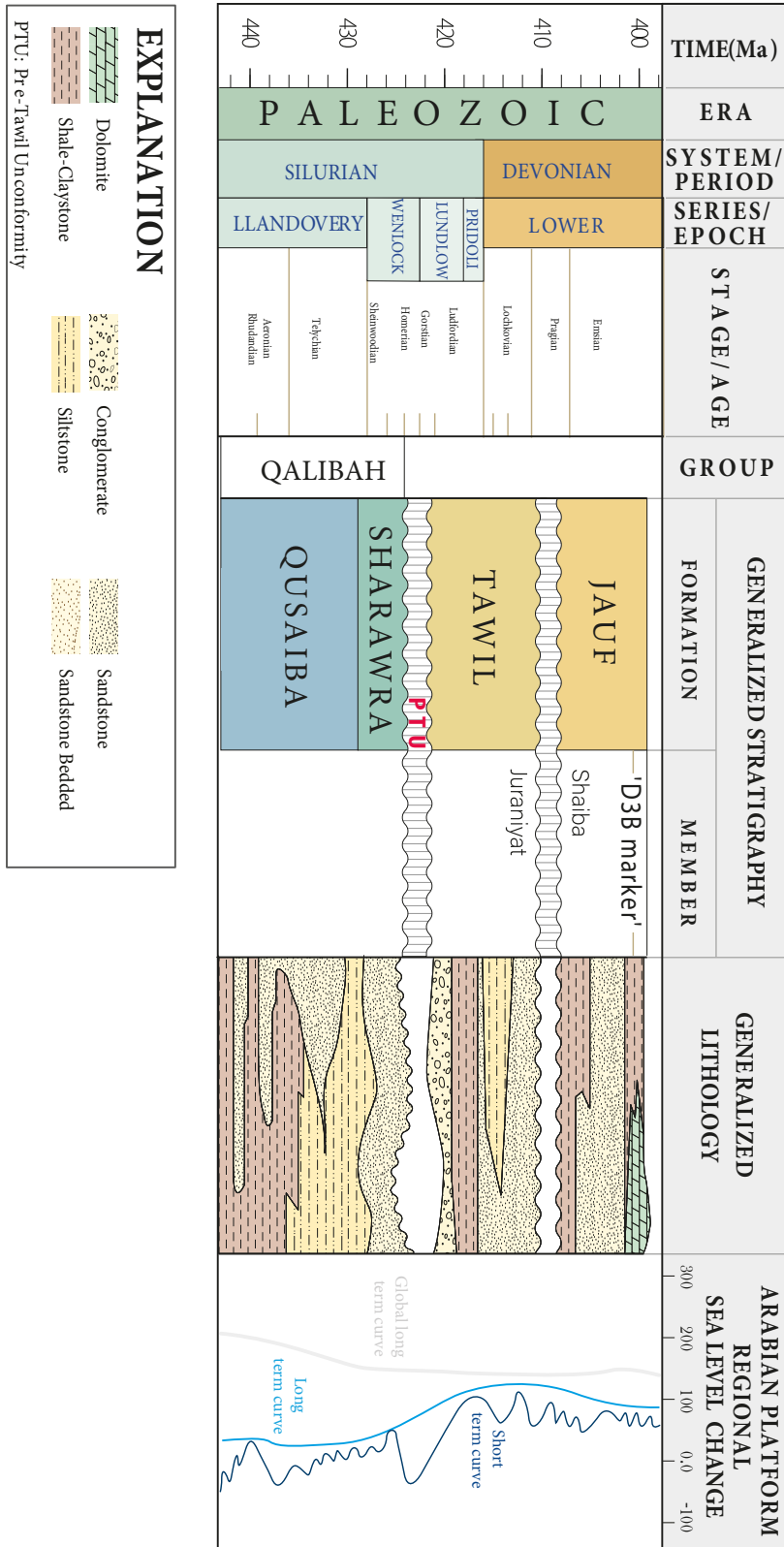
Figure 2. Lithostratigraphy and age constraint of the Sharawra, Tawil, and Jauf formations in Central Saudi Arabia.

preventing detailed biostratigraphic interwell correlation. The Tawil Formation does, however, extend down to the upper Silurian which can allow identification of the Tawil/Sharawra boundary. The Tawil Formation ranges from late Silurian (Ludlow) to early Devonian (early Pragian) in age and roughly coincides with the S1B-D4A palynological subzones (Mahmoud et al., 1992; Stump et al., 1995; Wender et al., 1998; Al-Hajri et al., 1999; Al-Hajri and Owens, 2000). On a palynological point of view, and in the same study wells, most of the samples were revealed barren and some of them yielded sparse spore species characterizing long range (Dossary et al., 2017).

1.3. Study material and analytical methods

1.3.1. Study material

The present study focuses mainly on the Silurian–Devonian section focusing on Tawil Formation. Samples have been also selected from the overlying Shaiba Member of the Jauf Formation and the underlying Sharawra Formation to allow characterization of the Tawil/Jauf and Tawil/Sharawra boundaries. In the present study, 663 samples were analyzed. The samples were finely ground and then fused using high-purity lithium metaborate flux (LiBO$_2$) and nitric acid (HNO$_3$) to 3.5%. The sample preparation is detailed in Soua (2016) with references therein. The samples were then analyzed using ICP-OES for major elements and ICP-MS for trace and rare earth elements to produce the dataset. The precision error for the major elements was less than 1% to 2% from the ICP-OES and between 3% and 5% for the ICP-MS. The accuracy error for the data is less than 1% for major and less than 5 ppm for trace elements.

1.3.2. Interpretive methods

The geochemical profiles were separated into two datasets including sandstone and mudrock to restrict the evaluation to similar litho-types. The aforementioned separation is made possible using the descriptions of core and cutting samples in combination with the Si/Al ratio in order to determine lithology. The samples producing Si/Al values less than 8 are considered as mudrocks and those yielding more than 8 are defined as sandstones. In general, elements Si and Al are concentrated mainly in quartz, and clay minerals with Si is the main component of Quartz. This ratio can generally model grain size.

Key elemental ratios, that demonstrate well-defined, repetitive signatures between wells or location were identified. These signatures were used to produce hierarchical correlations, including zones, subzones, and divisions, following the methodology of Pearce et al. (1999).

Some wells were not provided with gamma ray profiles and for data consistency, laboratory calculated GR has been elaborated for the lower part of Well-15-252, as well as for Well-608-465. The laboratory calculated GR is labeled in this study as Synthetic GR. It is calculated using the following formulas of Serra et al. (1980) and Ellis (1987):

Synthetic GR = 4 * Th ppm + 8 * U ppm + 16 * K%   (1)

2. Chemostratigraphic analysis and interpretation

2.1. Establishment of a relationship between elements and minerals

This is required to provide a framework for the chemostratigraphic analysis as sediments are defined by their composition and mineralogical content. Various controlling factors can influence the geochemical nature of a sandstone's composition and mineralogy, including provenance source composition, chemical weathering intensity, hydraulic action, diagenesis, etc. (McLennan, 1989; Fralick and Kronberg, 1997). Owing to the absence of detailed petrographic and XRD data, the geochemical data could not be directly compared with the sandstone mineralogy to establish these elemental affinities. It is possible to establish the element–mineral linkages by using statistical tools such as principal components analysis (PCA) and graphical techniques such as binary diagrams.

2.1.1. Statistical analysis and techniques

2.1.1.1. Aims and scope of the statistical techniques

Elements plotting together on the same field of data on an eigenvector (EV) could represent the potential of similar mineralogical affinities (Pearce et al., 2005; Svendsen et al., 2007; Ellwood et al., 2008; Ratcliffe et al., 2010; Sano et al., 2013; Soua, 2016). The principal component score of the elements on these eigenvectors indicate the relationship between the plotted elements and mineralogy.

In addition, discriminate function analysis (DFA) was possible by using UNISTAT software. DFA is a statistical method and used in this study to assess the levels of confidence associated with each defined chemozone. Generally, values exceeding 70% are acceptable.

2.1.1.2. Eigenvectors and principal components

In the absence of mineralogical data, PCA was used to establish element:mineral links. Many studies, based on comparison between geochemical and mineralogical data (Pearce et al., 1999, 2005; Mange and Morton 2007; Ratcliffe et al., 2010; Soua, 2016), have shown this to be a reliable methodology.

Principal components (PC) (Shaw, 2003) distills the number of variables into a smaller number of components. These PC values are derived from EVs, which provide a direction and magnitude to each element. These EV plots allow element groupings, using EV1 vs. EV2 and EV2 vs. EV3, from which element:mineral affinities can

be determined (Pearce et al., 2005; Svendsen et al., 2007; Ellwood et al., 2008; Soua, 2016).

EV1 and EV2 produce 86% of the total variation in the sandstone elemental concentration. Figure 3 and Table 1 summarize the PCA-derived EV plots for the sandstone elemental concentrations. It is inferred that elements grouping in the same data field are linked to the same group of minerals.

Figure 3 shows that the elements form six common group associations depicted through the eigenvector analysis when the EV1 and EV2 values are plotted:

I.   **Group 1:** Includes Al, Ga, Be, K, Rb, Cs, Cr, and Sr. These elements are associated with clay minerals, micas, and K-feldspars, although Cr is likely to be concentrated in heavy minerals but could be found in the clay, silt, and fine sand fractions.

Figure 3a. Eigen vector (EV) and Principal Component (PC) cross plots. A. EV1 vs. EV2 for data derived by PCA of all sandstone samples. B. PC1 vs. PC2. LREE: light rare earth elements, MREE: middle rare earth elements, HREE: heavy rare earth elements. All oxides have been abbreviated, e.g., Si = SiO$_2$. Color codes are used to differentiate the groups.
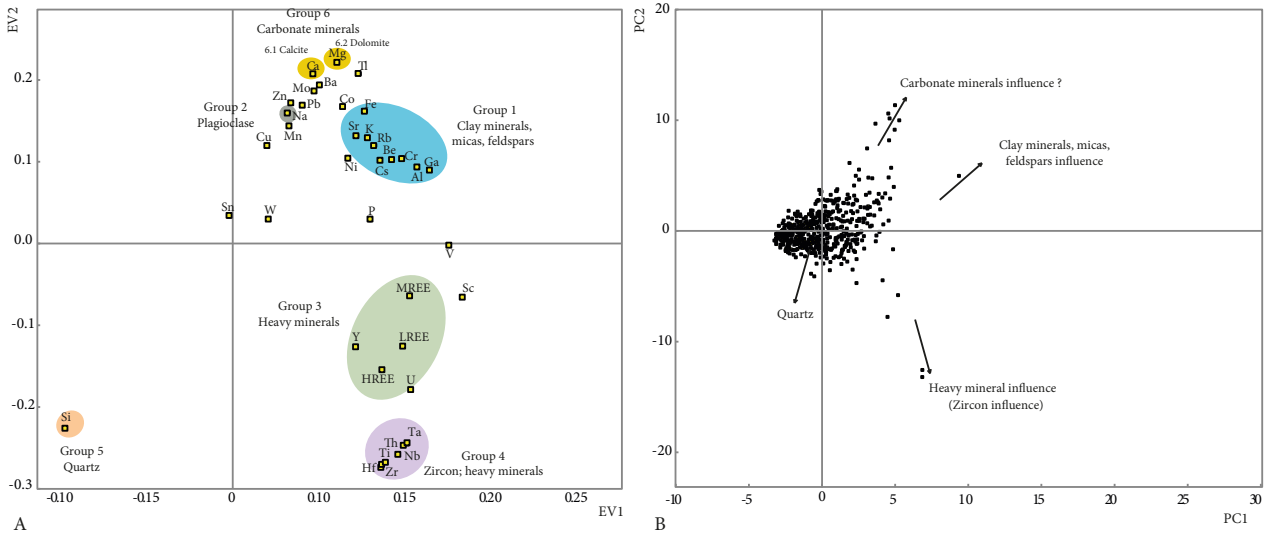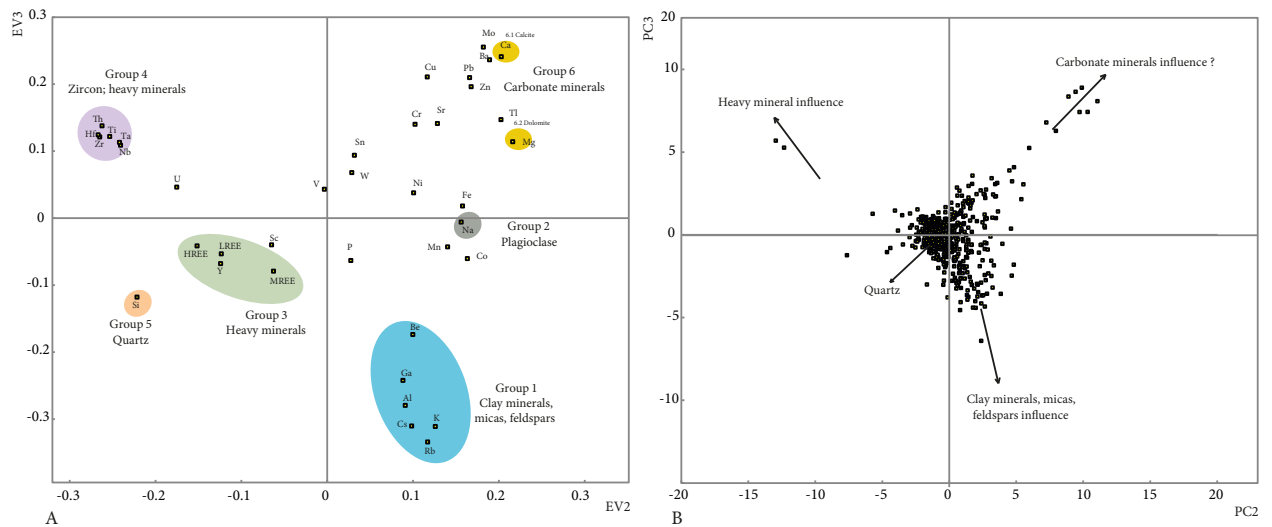

Figure 3b. Eigen vector (EV) and Principal Component (PC) cross-plots. A. EV2 vs. EV3 for data derived by PCA of all sandstone samples. B. PC2 vs. PC3.

Table 1. EV1 vs. EV2 crossplot and related groups of elements defined in this paper

Cross-plot	Groups	Group of elements	Mineral association
EV1 vs. EV2	Group 1	K, Sr, Rb, Be, Al, Cr, Cs, and Ga	Clay minerals, micas, feldspars
	Group 2	Na	Plagioclase (Albite)
	Group 3	LREE, MREE, HREE, Y, and U	Heavy minerals
	Group 4	Zr, Hf, Ti, Ta, Nb, and Th	Zircon and heavy minerals
	Group 5	Si	Quartz
	Group 6	Ca and Mg	Carbonate minerals (Calcite and Dolomite)

II.   Group 2: Includes Na, which is likely to have mineralogical affinities with plagioclase, although it can also occur in halite and smectite.

III.   Group 3: Includes all rare earth elements (light rare earth elements (LREE), middle rare earth elements (MREE), heavy rare earth elements (HREE)), along with U and Y. These elements are mainly concentrated in different suits of heavy minerals. According to Green and Pearson (1983) MREE and HREE are associated with titanite. In general, titaniferous heavy minerals contain Nb, Ti, and/or Ta (Schock, 1979). In this study, HREE and MREE do not plot in the same field as Ti and Nb, which suggests that they are not concentrated in titaniferous heavy minerals. The elements are found in high quantities in heavy minerals. Table 1 summarizes the EV1 vs. EV2 cross-plot and its related groups of elements.

IV.   Group 4: Includes Th, Ti, Nb, Ta, Zr, and Hf, which are linked with a variety of heavy minerals and share various mineralogical affinities (Morton and Hallsworth, 1994; Armstrong et al., 2005; Pearce et al., 2005). According to Fujimaki (1986) and Armstrong et al. (2005), Zr and Hf are mainly concentrated within zircon.

V.   Group 5: Si. This element is considered to be associated with quartz although it is an important contributor in clay minerals.

VI.   Group 6: Ca and Mg. Both elements are associated with carbonate minerals, such as calcite, dolomite, ankerite, and siderite. The element Mg could also be associated with ferro-magnesian minerals. The binary diagram (Figures 4a–4e) showed that a restricted relationship is present ($R^2 = 0.6$), which means that Ca is likely to be associated with calcite and Mg probably has multiple affinities including dolomite and some clay minerals such as chlorite.

Figure 3a shows that carbonate minerals (Group 6, Ca and Mg), clay minerals, mica and feldspars content (Group 1) mostly plot in the same field with high values of EV2. Eigenvector EV2 is affected by the variation of heavy minerals. This variation includes zircon, which plots with higher EV3 values, is indicative of decreasing grain size, since the Si (quartz) plots on the opposite side axis. The PC1 vs. PC2 binary diagram is also affected by carbonate, clay minerals, and heavy minerals including zircon.

The EV2 and EV3 plot shows associations of the aforementioned six groups (Figures 3a and 3b).

Figure 3b shows that the EV2 axis is influenced by three parameters including carbonate, clay minerals, and heavy minerals (Groups 3 and 4). The influences of carbonate, clay minerals, and heavy minerals including zircon are noted on the PC2 vs. PC3 binary diagram.

2.1.1.3. Elemental cross-plots
PCA analysis can be skewed by the presence of anomalously high or low values of a specific element measured from a low number of samples, which may result in erroneous interpretations.   Binary diagrams are therefore used to confirm or approximate the element:mineral linkages. If a strong correlation coefficient exists between two elements (R^2) the confidence is increased that it is a similar association (Pearce et al., 1999; Pearce et al., 2005; Ratcliffe et al., 2006; Soua, 2016). These diagrams are displayed in Figures 4a–4e.

The Al vs. Si crossplot (Figure 4a) shows a negative correlation coefficient between these two elements, reflecting the association of Si with quartz and Al with clay minerals. It is noted that a minority of sandstones and mudrocks plot with relatively low values of both elements, without forming a trend, which could be explained by carbonate dilution of clay and quartz. The Si vs. Ca graph (Figure 4a) shows that these samples plot with high values of Ca, which could be considered to be calcareous. Al vs. Ga ($R^2 = 0.95$) and K vs. Rb ($R^2 = 0.94$) graphs (Figure 4a), indicate strong correlation coefficients that could indicate that these elements are likely to be linked to clay minerals, K-feldspars, or micas. The positive trend displayed between Al and Ga suggests that both elements have same mineralogical affinities as they could be associated with clay minerals. In addition, the well-developed relationship between K vs. Rb can be explained by the fact that these elements are linked to K-feldspar, micas and/or clay
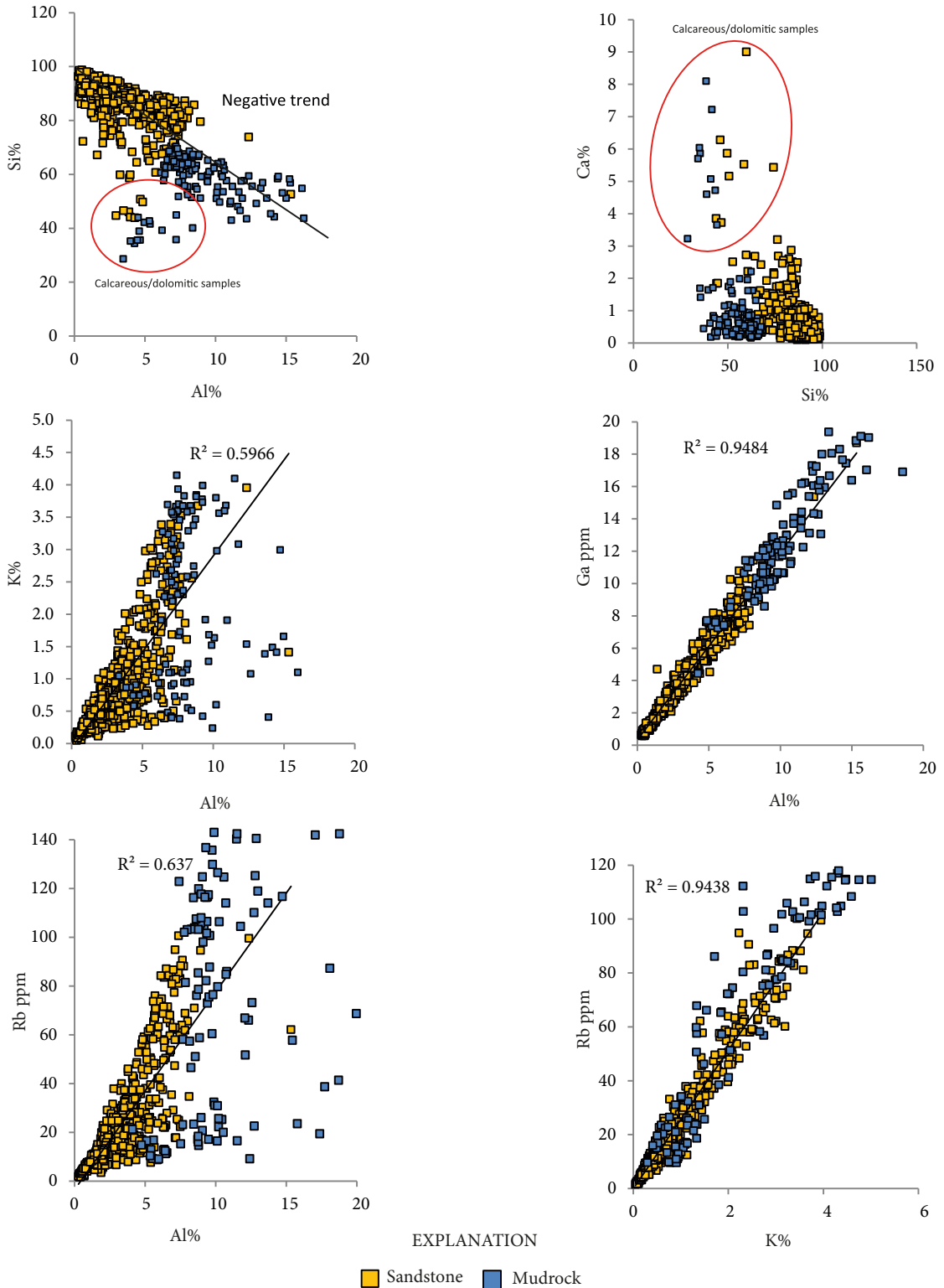
Figure 4a. Binary diagrams of selected elements. Color codes are selected to differentiate between sandstone and mudrock samples. R^2 is employed to either confirm or approximate the estimation of element:mineral linkages. This estimation is made possible when a strong correlation exists between two elements, which could indicate that a similar association is possible. To confirm a strong correlation between two elements values of R^2 should be in 0.75–1 range.
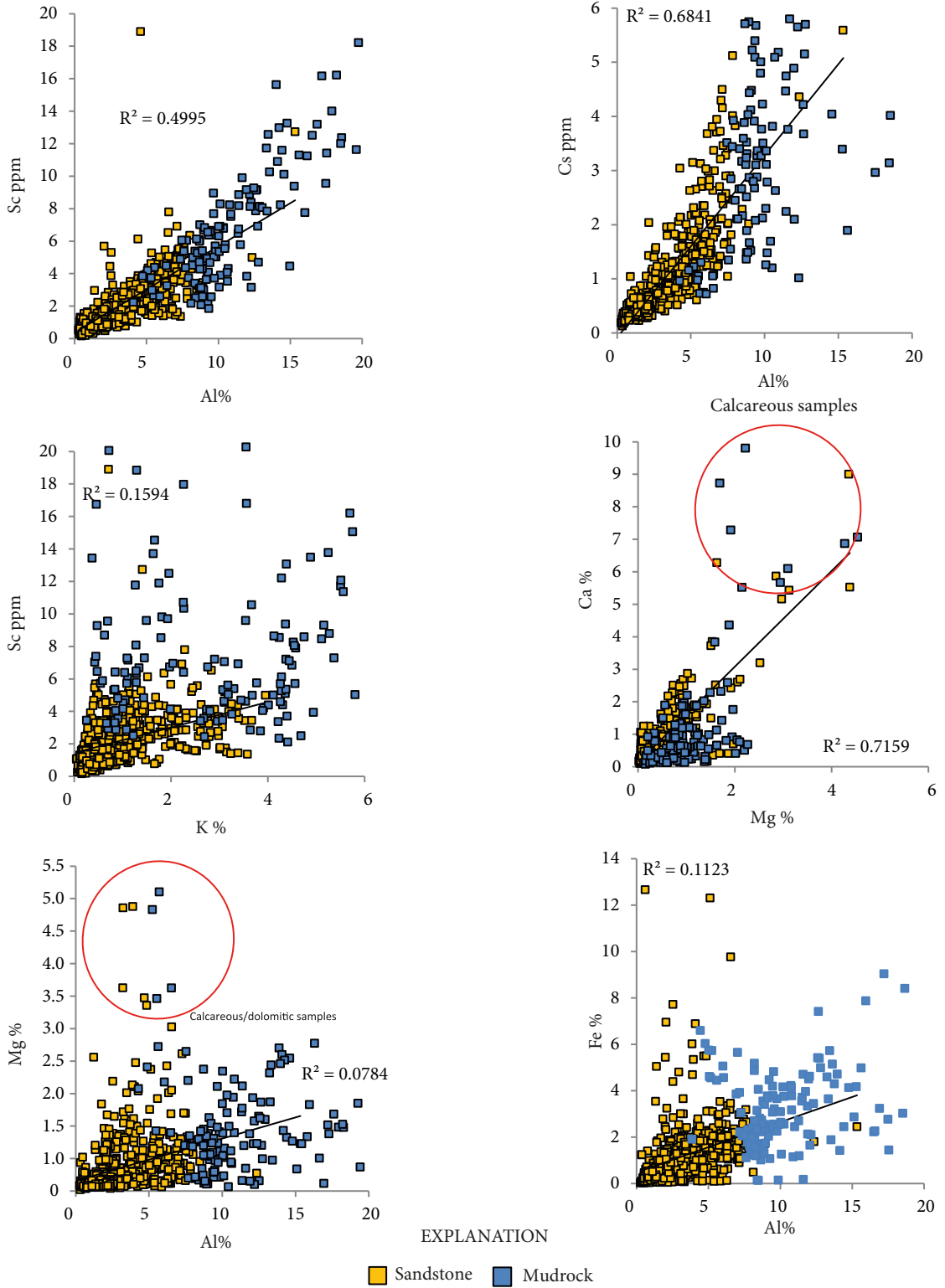
Figure 4b. Binary diagrams of selected elements (continued).
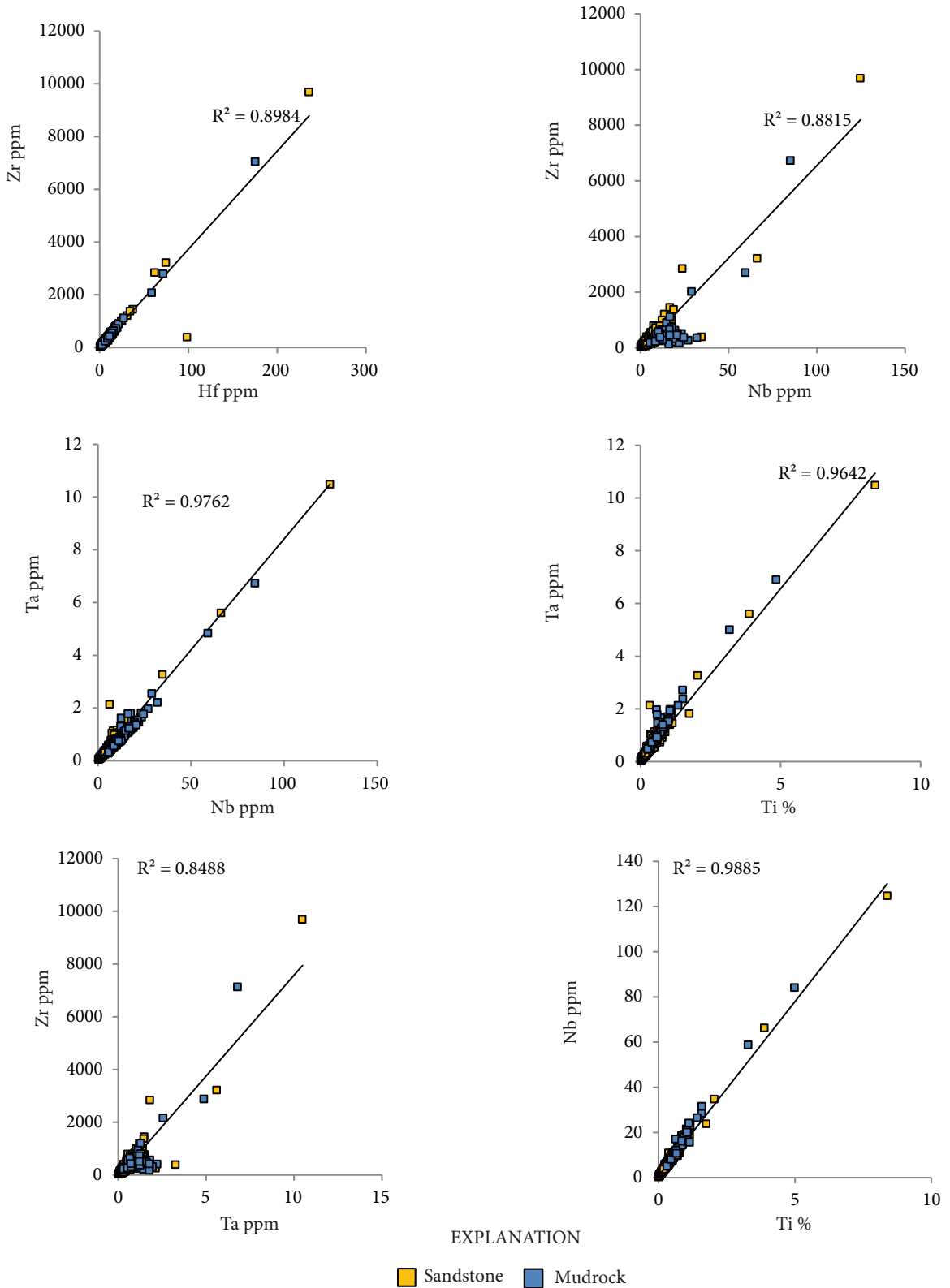
Figure 4c. Binary diagrams of selected elements (continued).
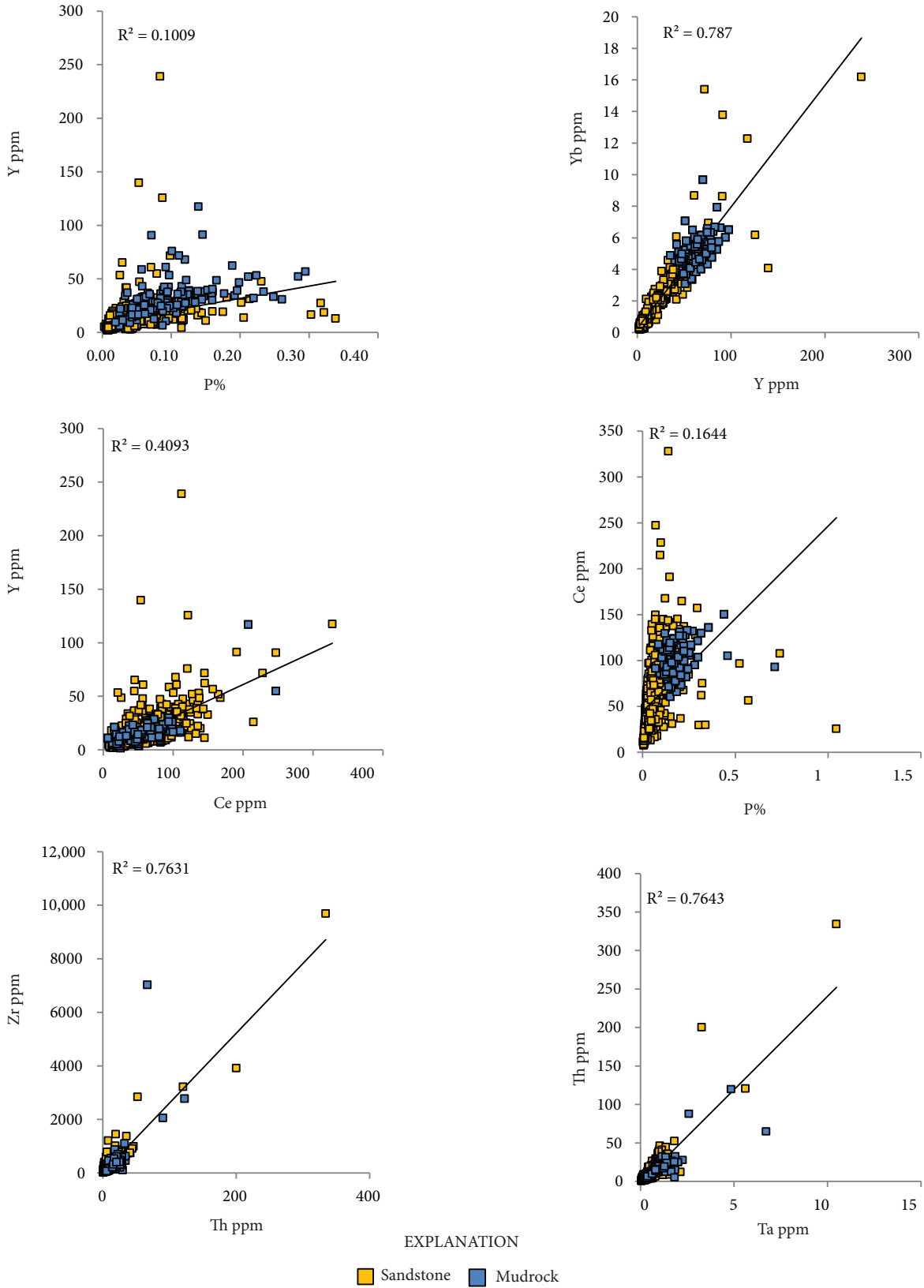
Figure 4d. Binary diagrams of selected elements (continued).
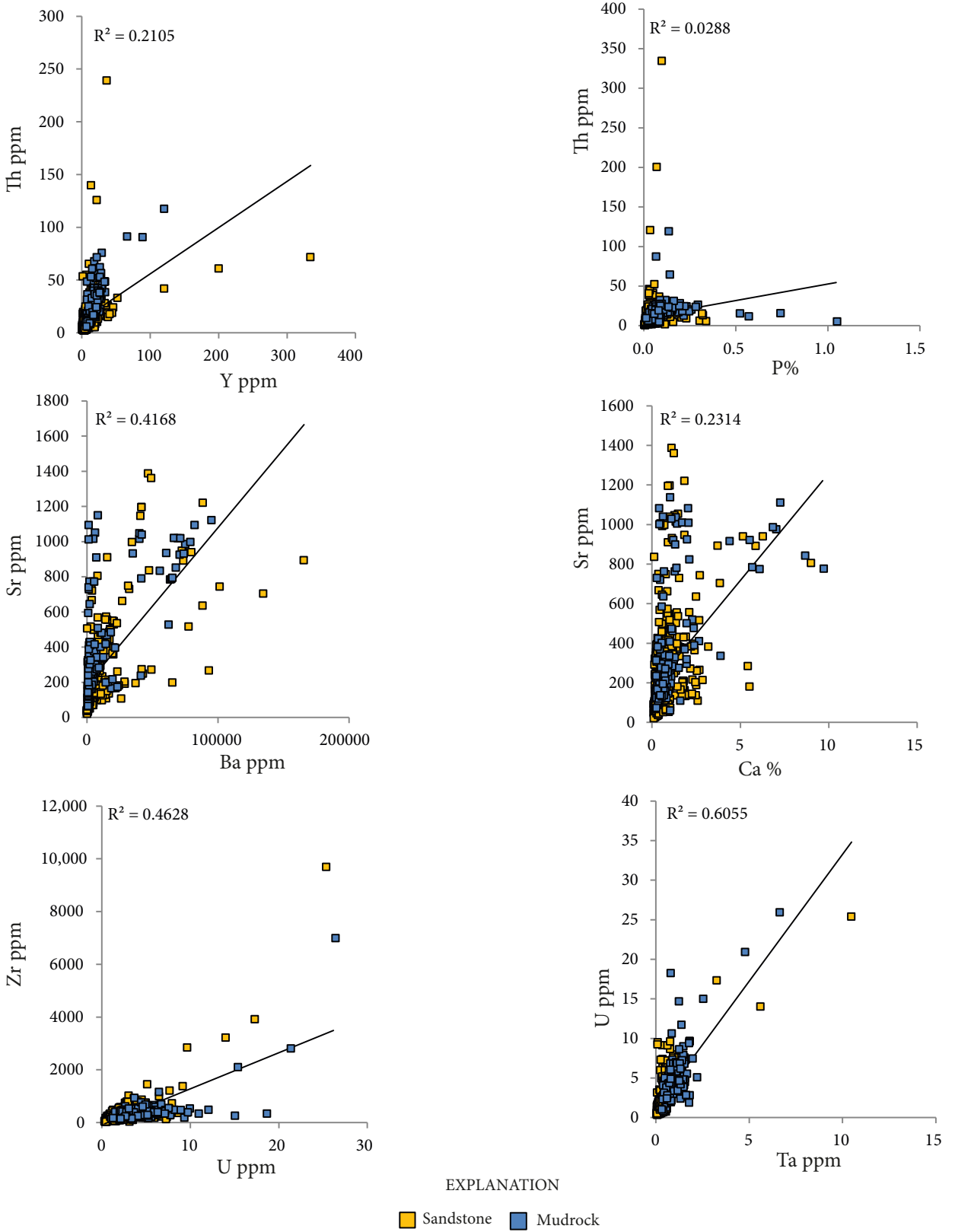
Figure 4e. Binary diagrams of selected elements(continued).

minerals. Alternatively, Figure 4a shows positive trends with lower correlation coefficient marked by Al vs. K (R^2 = 0.60), Al vs. Rb (R^2 = 0.64), Al vs. Cs (R^2 = 0.68) (Figures 4a and 4b). These elements are associated mainly with clay minerals, K-feldspar, and micas. The slightly lower correlation coefficient expressed in the Al vs. K graph could be explained by the fact that K and Al are largely concentrated in clay minerals with K generally associated with illite and/or K-feldspars, and micas. Al is linked generally to Al-bearing clay minerals such as kaolinite.

No significant relationship between Al and Mg (R^2 = 0.08) has been observed that could be explained by the fact that Mg is linked with carbonate minerals such as dolomite (Figure 4b). In addition, the lack of stronger correlation coefficient between both elements may be explained by the possibility that some Mg is associated with chlorite and Al with kaolinite. A moderate developed relationship between Mg and Ca (R^2 = 0.71) is also shown in Figure 4b. This suggests that both elements are associated with carbonate minerals. This moderate correlation could reflect that both elements are mainly concentrated in calcite and dolomite respectively or Mg in high Mg calcite and/or partly linked with clay minerals.

Al and Fe (R^2 = 0.11) shows a week developed relationship (Figure 4b). Such lack of relationship between Fe and Al could be explained by the fact that Fe may be associated with a variety of minerals including chlorite, pyrite Fe-oxyhydroxides and carbonate minerals such as siderite, where Al could be linked with kaolinite. In addition, there are moderate relationships developed also for Al and Sc (R^2 = 0.50) as well as for K and Sc (R^2 = 0.16). This infers that Sc contributes probably to the budgets of Al-bearing clay minerals, without any relationship to K-feldspars or micas (Figure 4b).

Figure 4c displays very good correlation coefficients developed between Ta, Ti, Nb, and Zr. The binary diagrams Nb vs. Ta (R^2 = 0.97), Ti vs. Nb (R^2 = 0.99), Nb vs. Zr (R^2 = 0.88), Ti vs. Ta (R^2 = 0.96) and Ta vs. Zr (R^2 = 0.85), suggest that these elements are associated with rutile, anatase, sphene, and/or opaque heavy minerals such as ilmenite, magnetite, and titanomagnetite and Zr is linked, almost exclusively, with zircons. A strong positive correlation coefficient exists between Zr and Hf (R^2 = 0.9). This was expected as these two elements are concentrated, almost exclusively, in zircon.

In addition, good relationships between Ta vs. Th (R^2 = 0.76) and Th vs. Zr (R^2 = 0.76) are shown in Figure 4d. This could suggest that Th may be associated with some heavy minerals. This may also indicate that some Th is associated with zircon. This positive correlation may indicate grain size trend, since the aforementioned elements are being associated with suits of heavy minerals.

Figure 4d also illustrates poorly developed trends between P vs. Y (R^2 = 0.1), Ce vs. Y (R^2 = 0.4) and P vs. Ce (R^2 = 0.16), while a stronger correlation coefficient is present between Y vs. Yb R^2 = 0.79). The poor coefficient developed between P and Y may be explained by the fact that P could be associated with apatite or monazite (phosphatic heavy minerals), instead of being associated with biogenic phosphate. This interpretation should be taken with caution, as the exact mineralogical affinities of P cannot be determined without the use of additional analysis such as heavy minerals or XRD diffractograms.

The element Ce as the majority of REE, as well as Y, are generally linked with a variety of heavy minerals.

Figure 4e shows less significant relationship developed between Ta and U (R^2 = 0.6), which may suggest that U shares different mineralogical affinities.

Similarly, a poor correlation between Th and Y (R^2 = 0.21) suggest that the two elements are unlikely to be concentrated in the same minerals (Figure 4e).

Figure 4e shows U vs. Zr and Ta vs. U binary diagrams. The well-developed correlation may indicate that these elements share a variety of heavy minerals.

Figure 4e also shows a poorly developed correlation between Ca and Sr (R^2 = 0.23). This can indicate that both elements do not share similar mineralogical affinities and may reflect the association of some Sr with carbonate minerals.

In addition, several trends between Ba and Sr are highlighted. Stronger positive trend represents probably association with drilling additives.

2.1.1.4. Summary of element:mineral links
Element:mineral links can be summarized and integrated with mineralogical, statistical data, and published studies (e.g., Pearce et al., 1999; 2005; Ratcliffe et al., 2006; 2008). Tables 1 and 2 summarize the element:mineral affinities. Table 3 shows the DFA confidence of the produced chemozones.

2.2. Chemostratigraphy interpretation
2.2.1. Key elemental ratios
Annex tables (Annex 1 to Annex 5) show min, max, and average values of the five study wells provided by chemozones. The proposed chemostratigraphic workflow uses elemental-ratio data to model changes in provenance in order to provide a high-resolution correlation, except (Rb+Cs)/La and Al/(Ca+Mg+K+Na), which are used to recognize weathering and diagenesis. Alternatively, the proposed workflow is based on variations in 13 key elements and 7 key elemental ratios. The key element ratios and their mineralogical characterization are detailed below and summarized in Tables 1 and 2.

Table 3. Results of DFA applied at the zone level.

	C1	C2	C3	C4
C1	115	9	3	2
	89%	7%	2%	2%
C2	2	82	24	8
	2%	71%	21%	7%
C3	5	29	148	3
	3%	16%	80%	2%
C4	2	11	9	73
	2%	12%	9%	77%

Correctly classified: 86%

Variations in Zr/Nb, (Zr*Hf)/(Nb*Ta), (Zr*Hf)/Nb, and Zr/(Nb*Ta) were mainly used in this study (Figures 5a–5c), reflecting changes in provenance and source area. These elements are associated with a variety of heavy mineral suites and are largely indicative of variations in zircon (Fujimaki, 1986), Ta- and Nb-bearing heavy minerals (i.e., rutile, anatase, sphene, titanomagnetite, magnetite, ilmenite) (McLennan, 1989; Figures. 3a–3b, Table 1). These are ultrastable heavy minerals (Pettijohn et al., 1987) and, therefore, are not affected by weathering/ diagenesis. The binary diagrams confirm these associations (Figures 4a–4e). Close inspection of the PCA analysis (Figures 3a and 3b) shows that Nb is associated with Ti, Ta, Th, Zr, and Hf (Group 4). In general, Zr and Hf occur in zircon; Ti, Ta and Nb are associated with rutile anatase, sphene ilmenite, titanomagnetite and/ magnetite (Morton and Hallsworth, 1994; Armstrong et al., 2005; Pearce et al., 2005). Th is generally associated with monazite (Mange and Morton, 2007), but it could also be concentrated in zircon, apatite, and opaque heavy minerals with variable concentrations.

Consequently, changes in provenance trends show significant variations in Zr/Nb, Zr/Th (Zr*Hf)/(Nb*Ta), (Zr*Hf)/Nb, and Zr/(Nb*Ta) elemental ratios as illustrated in Figures 5a–5c. Figure 6 shows the signature variation of the key elemental ratios from well to well, from which we can infer that the wells location with respect to the source also needs to be considered. The ratios (Rb+Cs)/La and Al/(Ca+Mg+K+Na) were also used in this study. Figures 3a–3b shows that Rb and Cs plot in the same group, Group 1, which is mainly linked to clay minerals (illite), micas, and K-feldspars (e.g., Riboulleau et al., 2014;). It is difficult to provide the exact mineral affinity of La, but this element is known to be concentrated in a set of heavy minerals

Table 2. Elements and their mineralogical affinities

Elements	Ratios	Comments
Zr, Nb	Zr/Nb	Zircon vs. Nb-bearing heavy minerals (i.e. rutile, anatase, ilmenite, sphene, magnetite)
Nb, U	Nb/U	Nb-bearing heavy minerals vs. U-bearing heavy minerals
Al, Ca, Mg, K, Na	Al/(Ca+Mg+K+Na)	Weathering indicator
Zr, Hf, Nb, Ta	(Zr*Hf)/(Nb*Ta)	Zircon vs. Nb and Ta-bearing heavy minerals (e.g., magnetite, illmenite, rutile, anatase, and/or sphene)
Zr, Hf, Nb	(Zr*Hf)/Nb	Zircon vs. Nb-bearing heavy minerals (e.g., rutile, anatase, ilmenite, sphene, magnetite)
Zr, Nb, Ta	Zr/(Nb*Ta)	Zr vs. Nb and Ta-bearing heavy minerals (e.g., magnetite, illmenite, rutile, anatase, and/or sphene)

Figure 5a. Chemostratigraphic correlation proposed for Well-608-1009 and Well-15-252. Geochemical data acquired for sandstone core samples were used to construct this scheme. The correlation scheme is based on the chemical signature provided by the generated chemozones C1, C2, C3 and C4 as well as their related subzones C2-1, C2-2, C2-3 C3-1 and C3-2 in ascending order. Biostratigraphy subzones as well as revised lithology are plotted.

such as monazite. Therefore, the ratio (Rb+Cs)/La can provide information on clay minerals, micas, K-feldspars vs. is La-bearing heavy minerals. Although La can occur in

heavy minerals, including monazite, it could also be linked with feldspar and clay minerals. The Al/(Ca+Mg+K+Na) ratio is used as a weathering indicator (Pearce et al., 2005;
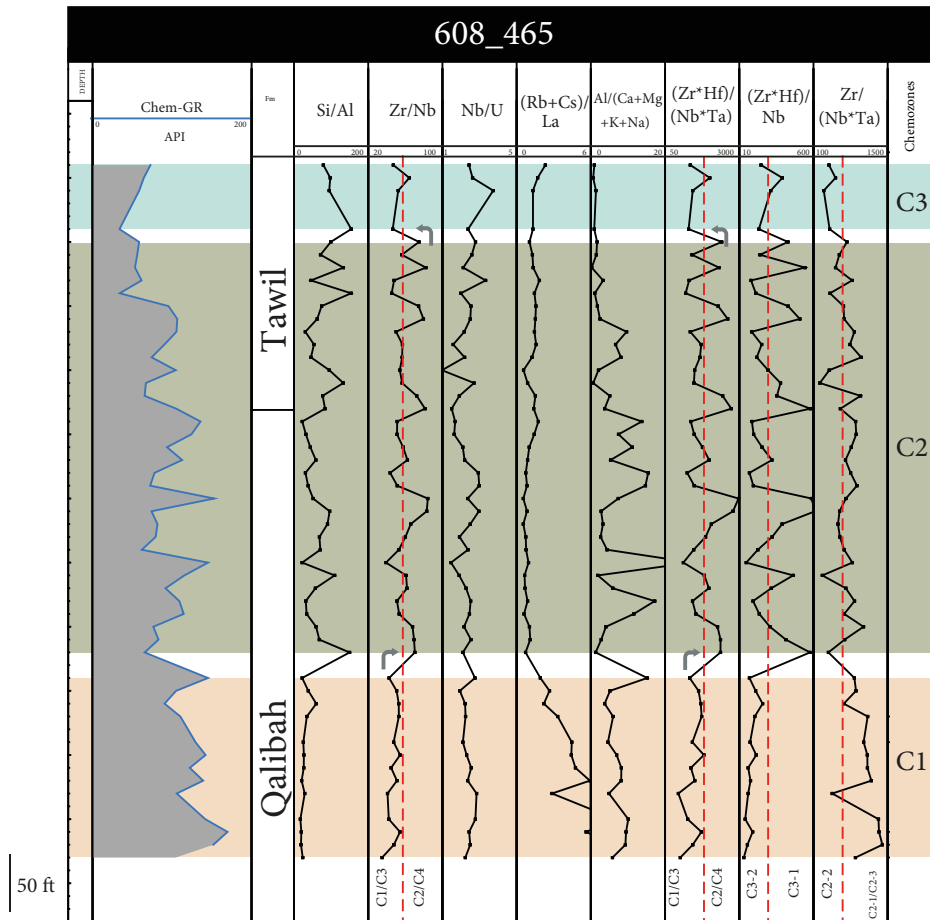
Figure 5b. Chemostratigraphic analysis for Well-608-465.

Ratcliffe et al., 2010; Soua, 2016). Consequently, the Al/ (Ca+Mg+K+Na) ratio is used for chemostratigraphic purpose to define weathering surfaces and possible unconformities but not to define chemozones.

2.2.2. Chemostratigraphic analysis
In the present study, a workflow was developed to subdivide sandstone strata into zones and subzones (Figures 5a–5c), based primarily on changes and variations in the key elemental ratios (Table 2).

Figures 5a–5c show the correlation output based on this workflow. The Si/Al ratio is plotted along with key elemental ratios to model quartz vs. clay minerals. Aluminum is associated with clay minerals including kaolinite. The high concentration of Al can reflect decrease in grain size, while low values can be indicative of increase in grain size. The purpose of plotting the Si/ Al ratio is to constrain the variation in grain size. The correlation panels are shown in Figures 5a–5c.

The cross-plots of Figures 7a–7b summarize the differentiation of zones and subzones recognized in the sandstone dataset.

The values of cut-offs are used to define individual chemozones and subzones within the correlation. These values have been recognized by examining the geochemical profiles and verified by binary diagrams of Figures 7a and 7b (plotted for each well). From the sandstone dataset, a well-defined hierarchical order of zones and subzones was constructed. A chemostratigraphic workflow was not established for the mudrock dataset because of the small number of samples. The chemostratigraphic correlation workflow is discussed in the following sections.

2.2.2.1. Chemostratigraphic zones
Four chemostratigraphic zones have been identified in this study from the sandstone dataset. These zones are labelled C1, C2, C3, and C4 in ascending stratigraphic order. Zones C1 and C3 have lower Zr/Nb and (Zr*Hf)/ (Nb*Ta) values than in Zones C2 and C4.

The sandstones of zone C1 can be generally differentiated from those of the overlying C2 by their lower Zr/Nb and (Zr*Hf)/(Nb*Ta) values (Figures 5a– 5c). In Well-608-215, this is less clearly defined and only a tentative differentiation between C1 and C2 is possible.
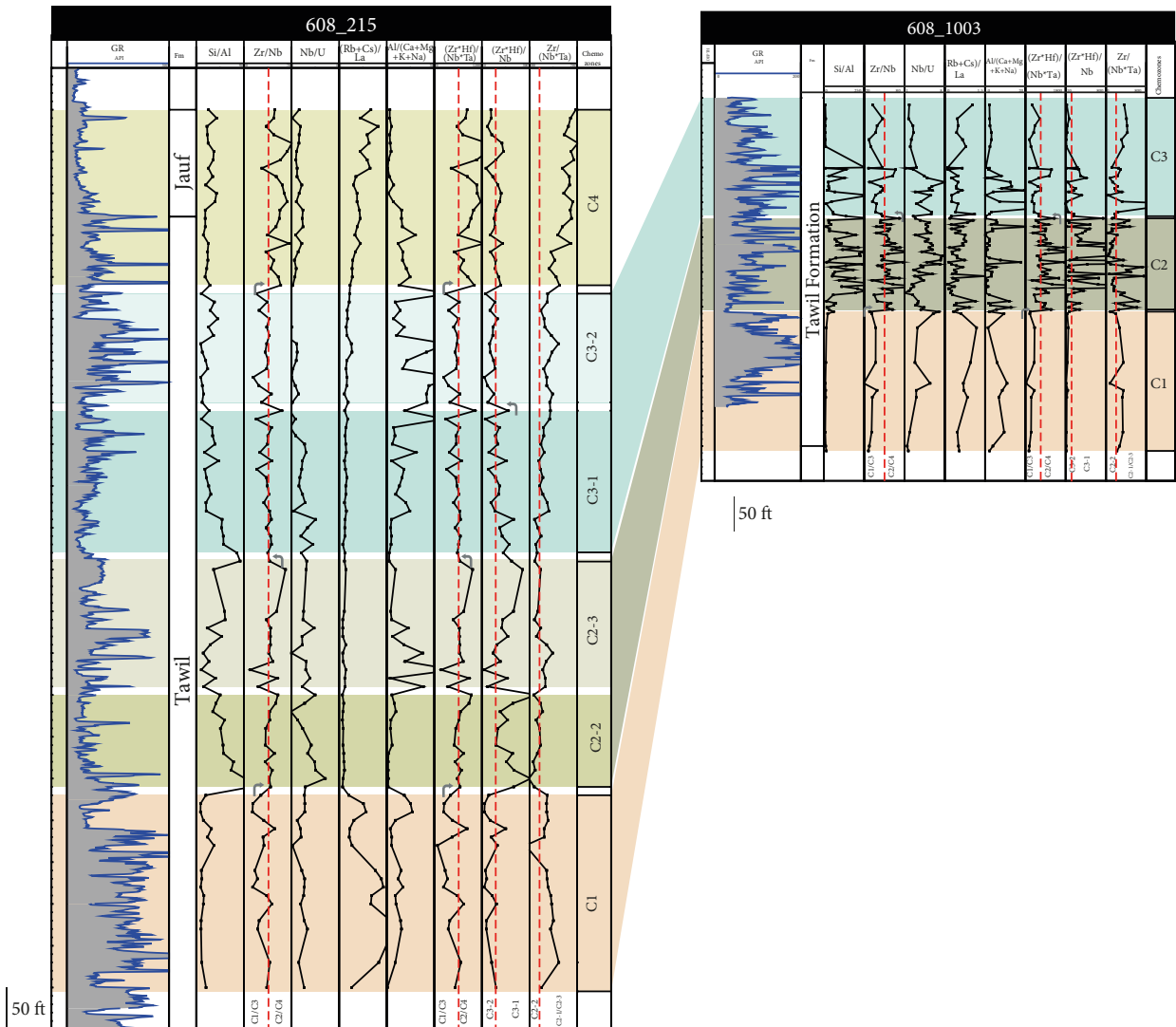
Figure 5c. Chemostratigraphic correlation proposed for Well-608-1003 and Well-608-215. Note that C2-1 is probably absent due to the pre-Tawil unconformity, which marks the boundary between the base of the Tawil Formation and underlying older units (Silurian to Late Ordovician, Sharawra, Qusaiba and Sarah formations). This unconformity is attributed to the Acadian tectonic movement (Laboun, 2010).

Zone C2 is roughly equivalent to lower Tawil Formation. The sandstones of zone C2 have Zr/Nb and (Zr*Hf)/(Nb*Ta) values that are significantly higher than those of C1 and C3 but less pronounced than those of zone C4 (Figure 6).

The differentiation of chemozones is shown in Figures 5a–5c. Figure 6 summarizes the principal characteristics of each chemozone. In addition, the differentiation of zones and subzones are presented in the binary diagrams of Figures 7a and 7b. Beacause of the small number of samples given to both subzones and divisions, these cross-plots have only been utilized to differentiate chemozones.

In general, the crossplots enable the characterization of the identified chemozone, and to confirm the placement of the boundaries.

Table 3 shows that DFA produces confidence of 86%. This reflects that 89% of the zone C1 samples and 80% of the zone C3 have been correctly placed in the chemozones.

In addition to DFA, binary diagrams are used for the same purpose utilizing Zr/Nb and (Zr*Hf)/(Nb*Ta) ratios (Figures 7a and 7b). For example, zone C1 is defined by Zr/Nb values of lower than 50 and (Zr*Hf)/(Nb*Ta) values lower than 625 while Zone C2 is characterized by Zr/Nb and (Zr*Hf)/(Nb*Ta) values of higher than 50 and

C1
Zr/Nb < 50
(Zr*Hf)/(Nb*Ta) < 750[*]

C2
Zr/Nb > 50
(Zr*Hf)/(Nb*Ta) > 750[*]

C3
Zr/Nb < 50
(Zr*Hf)/(Nb*Ta) < 750[*]

C4
Zr/Nb > 50
(Zr*Hf)/(Nb*Ta) > 750[*]

C-21
Zr/(Nb*Ta) > 400

C-22
Zr/(Nb*Ta) < 400

C-23
Zr/(Nb*Ta) > 400

C31-
(Zr*Hf)/Nb > 60[**]

C32-
(Zr*Hf)/Nb < 60[**]

[*] cutt off value of   62 5 for (Z r*Hf)/(Nb*Ta) use   d in Well 15-252

[**] cutt off value of   10 0 for (Z r*Hf)/Nb use d in Well 15-252

Figure 6. Principal geochemical characteristics of zones C1, C2, C3, and C4 and associated subzones (C2 and C3).

Figure 7a. Binary diagrams used to differentiate zones C1, C2, C3, and C4 in wells Well-15-252 and Well-608-215.

Figure 7b. Binary diagrams used to differentiate zones C1, C2, C3, and C4 in wells Well-608-1009, Well-608-1003, and Well-608-465

625, respectively. Figures 7a and 7b show that almost all of the zones produce good levels of confidence with more than 70% of samples plotting in the correct field (Figure 8). The histograms show that thi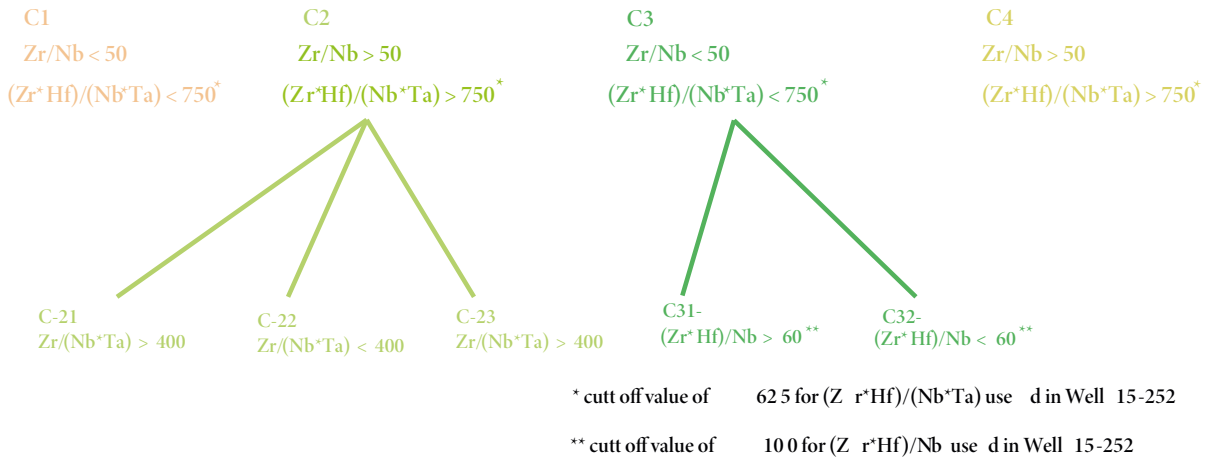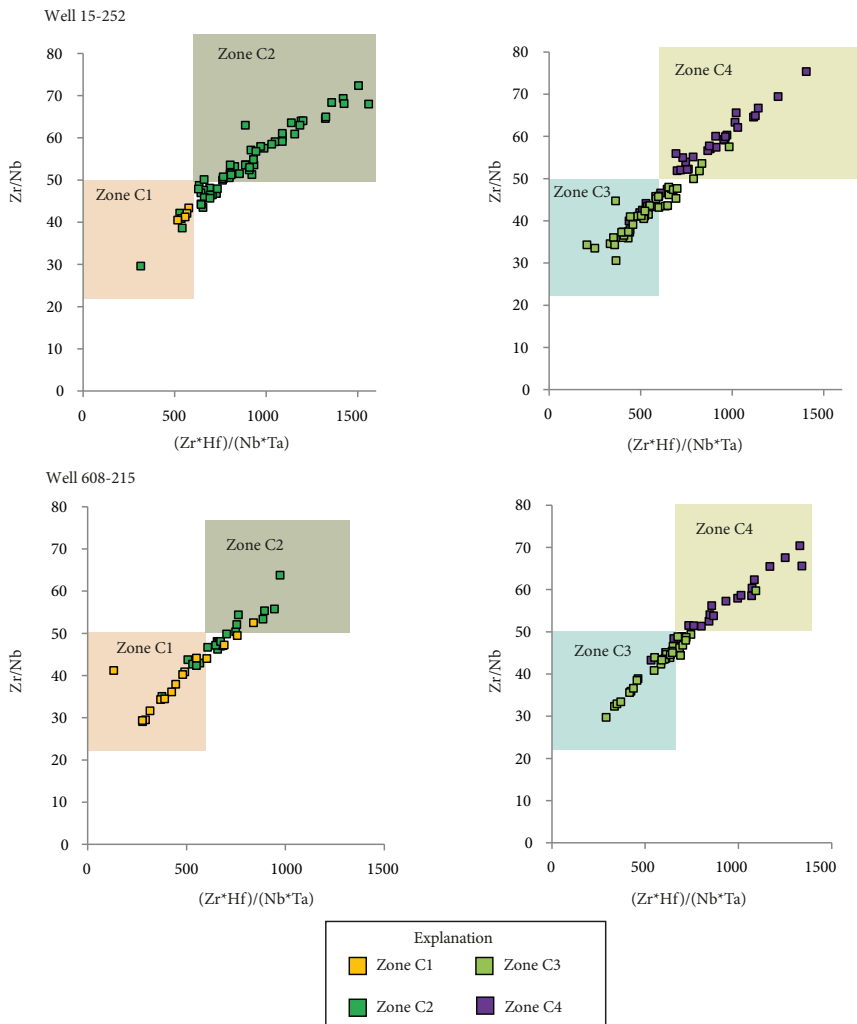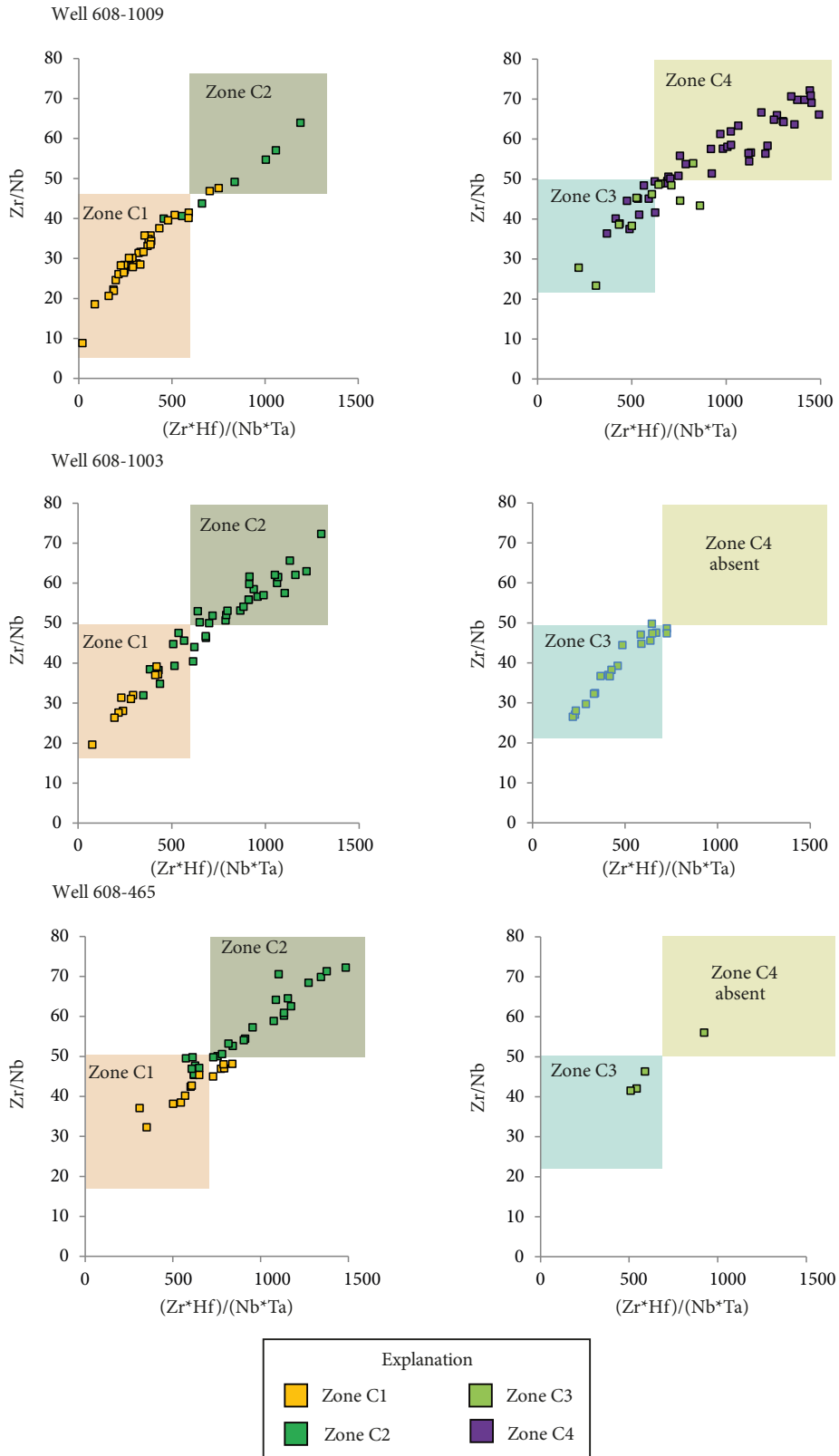s holds true for around 95% of the samples assigned to this zone. Similarly, more than 80% of the C3 samples yield Zr/Nb of less than 50 and (Zr*Hf)/(Nb*Ta) values of lower than 625. As a general rule, zonation confidence is considered to be high where more than 70% of the samples are correctly assigned to the correct chemozone (Figures 5a–5c). Figure 9 summarizes the correlation workflow produced for the five study wells. Figure 10 shows that almost all of the zones produce levels of confidence of greater than 70%. Moderate–high levels of confidence typify the range 60%–70%, while moderate and low levels of confidence are defined by the ranges 50%–60% and below 50%, respectively.

2.2.2.2. Chemostratigraphic subzones

Chemostratigraphic subzones are recognized in zones C2 and C3 where threefold and twofold subdivisions are proposed respectively. Subzones C2-1 and C2-3 are characterized by higher Zr/(Nb*Ta) ratios than in the intervening subzone C2-2. The C3 subzones, labelled C3-1 and C3-2 in ascending stratigraphic order, are differentiated by the former producing higher (Zr*Hf)/Nb values. Figure 6 summarizes the principal geochemical characteristics of each subzone. In summary, the differentiation of subzones is shown in Figures 5a–5c and in the cross-plots of Figures 7a and 7b.

3. Discussion

3.1. Chemostratigraphic correlation

Figures 5a–5c present the detailed chemostratigraphic workflow for the sandstone dataset, summarized in Figure 9. This diagram shows the chemostratigraphic zonation (zones and subzones) and a comparison with lithostratigraphic subdivisions, palynological zones and established formations (Sharawra, Tawil, and Lower Jauf).

Based on data analysis in the current study, Zone C1 is generally associated with the Sharawra Formation, in Well-15-252, while it is associated with Tawil in wells 608-1009, 608-1003, and 608-215 (Figure 9). Zones C2 and C3 are linked with the Tawil Formation, and Zone C4 broadly defines the Jauf Formation. Chemostratigraphic zonal boundaries do not precisely correspond to biostratigraphical and formational boundaries (Figures 9 and 10), indicating probably that the C1-C2 and C3-C4 boundaries are time-transgressive. This suggests that the aforementioned lithostratigraphic units were probably deposited in multiple fluvio-deltaic systems, fed by sediments from the same clastic sources, active at different times (Janjou et al., 1997; Rahmani et al., 2002;

Laboun, 2010; Dossary et al., 2017). This can be supported by the sedimentological interpretation of the same wells, which confirms that the environment of deposition is mostly represented by fluvial distributary channels tidally influenced within an overall deltaic setting (Dossary et al., 2017).

In general, four chemostratigraphic zones, namely (in ascending order) C1, C2, C3, and C4 are defined for the Silurian–Devonian section (Sharawra, Tawil and Jauf formations) from five wells (Figure 9). Additionally, in this study, biostratigraphic (palynology) and lithostratigraphic data have been compiled from Dossary et al. (2017) to allow reliable correlation at regional scale (Figure 9). The correlation panels have been produced regionally (Figures 5 and 9). Dossary et al. (2017) discussed that most of the studied samples from the same wells were either barren or yielded sparse spore species characterizing long range.

In Well-15-252, Zone C1 is generally related to the upper Silurian and is separated from the overlying chemozone by the pre-Tawil unconformity, representing a time break (Ludlow to the Wenlock) without a sharp erosive surface in eastern Saudi Arabia (Helal 1965; Bigot 1970; Al-Hajri and Paris, 1998; Al-Ramadan et al., 2004). Alternatively, Laboun 2010 related this regional uplift event and erosion to the Caledonian orogeny. This implies that similar mechanisms existed in North Africa where a coeval time gap has been described in Ghadames Basin being attributed also to the Caledonian unconformity (Soua, 2014).

Geologically, the Tawil Formation is characterized by relatively coarse-grained sandstones, being differentiated from the underlying Sharawra Formation, which contains mainly silty sandstones with significant amounts of feldspars and micas (Rahmani et al., 2002). Dossary et al. (2017) confirmed that with integration of biostratigraphic, chemostratigraphic, and sedimentological data, the Tawil Formation is more siliciclastic and mostly represent fluvial sandstones, in southwest and western area, while toward the north and northeastern more distal facies are located.

In Zone C2, the geochemical change in the Zr/Nb ratio as well as in Zr*Hf/Nb*Ta, Zr*Hf/Nb and Zr/Nb*Ta parameters may reflect high zircon/rutile, anatase, sphene, and other heavy mineral ratios. The geochemical and mineralogical changes shown in this zone are in agreement with Cocker et al. (2003), who differentiated the sandstones of Jauf and Tawil Formations based on the euhedral zircon index (eZi), being concentrated with high values in the latter (around 4 on average). The euhedral zircon index is commonly used as provenance indicator, where high eZi values could be associated with provenance source area being provided from the basement directly rather than from reworked sediments. The major change
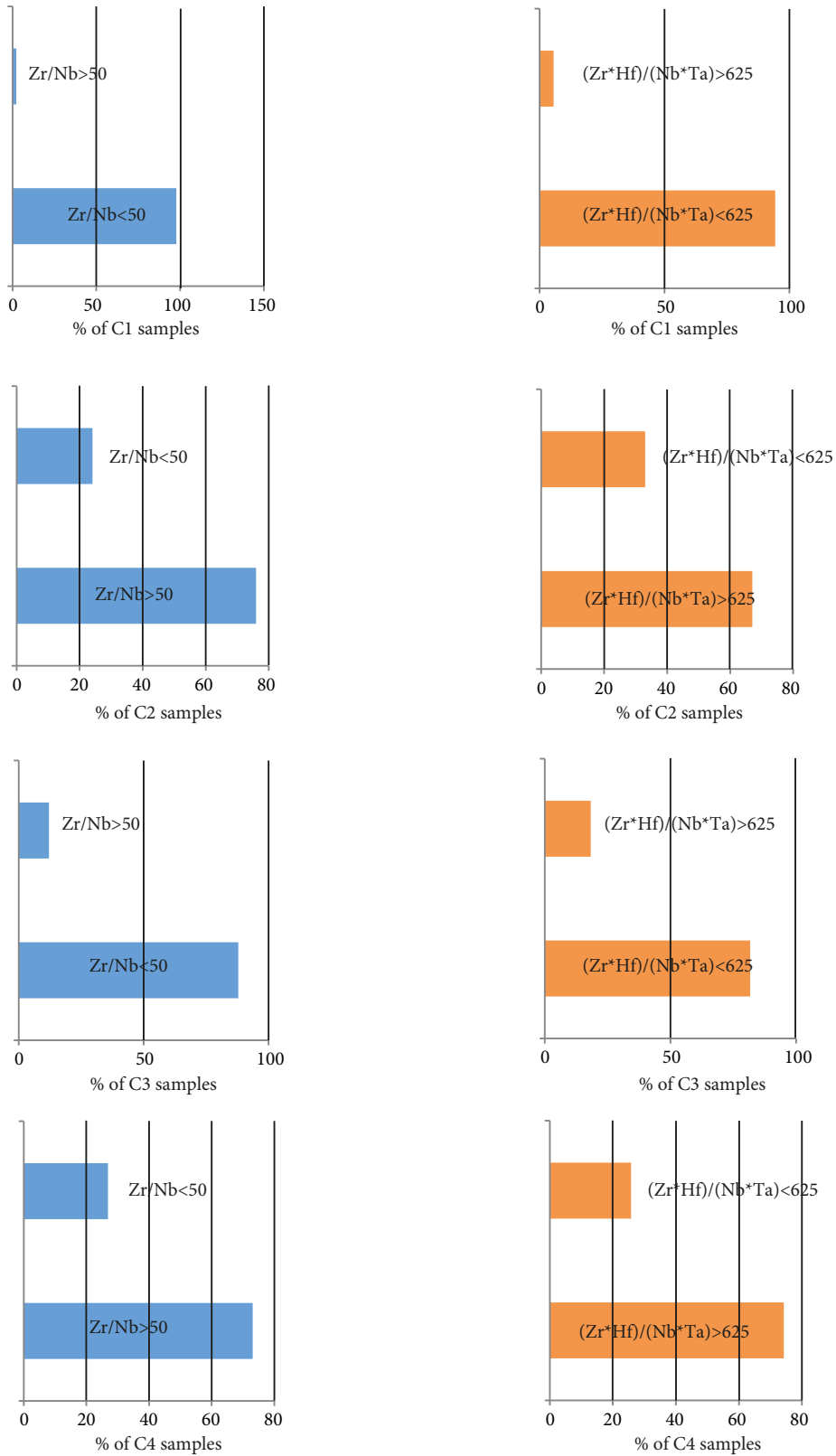
Figure 8. Histograms used in this study to predict zonation confidence with respect to chemostratigraphic zones.
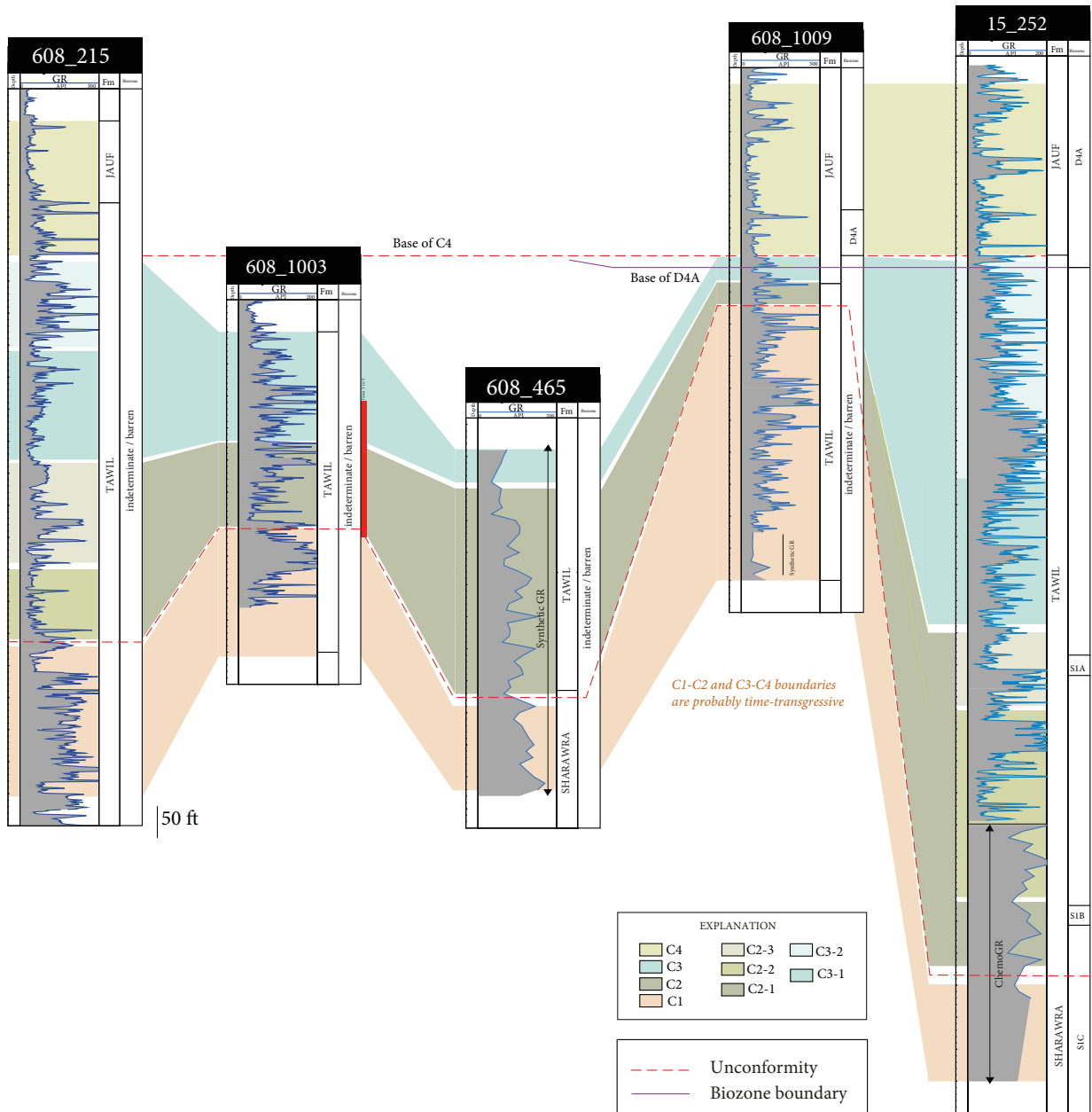
Figure 9. Summary of chemostratigraphic correlation. All depths are log depths in feet. Silurian–Devonian biozones are integrated. Color codes are selected to differentiate between the generated chemozones and related subzones.

seen in values range of the Zr/Nb, Zr*Hf/Nb*Ta, Zr*Hf/Nb, and Zr/Nb*Ta ratios could be linked to the change of the source area (from reworking source to basement for example). In general, Zone C3 is roughly equivalent to the upper part of the Tawil Formation but is not recognized in Well-608-465, where it may not have been penetrated. In all the wells where it is differentiated, it is lithologically variable. The C3:C4 boundary roughly coincides with the probable pre-Jauf unconformity in Well-15-252 (Figure 5a). The sandstones of zone C3 have low Zr/Nb values

that are similar to those encountered in zone C1 (Figure 6), inferring that both zones may have a similar source/provenance. Interestingly, zone C3 is also characterized by generally higher Al/(Ca+Mg+K+Na) values, which could be interpreted as intensified weathering of the sandstone related to paleosol levels developed within the Tawil Formation.

In Well-608-465 and Well-608-1003, Zone C3 could not be subdivided into subzones (C3-1 and C3-2). Zone C4 is roughly equivalent to the lower part of the Jauf Formation

but is not recognized in Well-608-465 and Well-608-1003; most likely because the section was not penetrated.

3.2. Integration of stratigraphic data

3.2.1. Stratigraphy and dating

Figure 10 summarizes the lithostratigraphy along with the biostratigraphy of the study wells. According to Dossary et al. (2017), the oldest palynological biozone identified in the same study wells is associated with Devonian (Lochkovian). Figure 9 shows that, palynologically, two palynosubzones are present including D4B characterizing the upper part of the Tawil Formation, and D4A (Pragian-early Emsian) spanning the Tawil/Jauf boundary (Figure 9). The lower limit of the Tawil Formation is marked by the pre-Tawil unconformity while the upper limit with the Jauf Formation is probably disconformable.

3.2.2. Sequence stratigraphy modelled from elemental data

According to Sano et al. (2013), the ratio Zr/Nb can vary in proportion to grain size. In general, the element Zr is associated with zircon heavy mineral; while Nb is often associated with Nb-bearing heavy minerals but can also be associated with clay minerals, usually likely to be present with illite. Following Figures 3a and 3b, Nb plots in association with Group 4, including Ta, Ti, Th, Zr, and

Figure 10. Construction of the correlation scheme and relationship with the lithostratigraphy and biostratigraphy. The correlation scheme is based on four chemozones C1, C2, C3 and C4 as well as their related subzones C2-1, C2-2, C2-3 C3-1 and C3-2 in ascending order. Lithostratigraphy and Biozones are plotted.

Hf, and displays a strong correlation coefficient with these elements, which mark the variation of heavy mineral content of the silty clays (Sano et al., 2013). Therefore, the Zr/Nb ratio could be used as a good indicator for grain size.

Generally, a transgressive sequence is characterized by a fining upward interval, terminated by a maximum flooding surface (MFS), while a coarsening upward interval defines generally a regressive/prograding sequence, which could represent generally sequence boundaries (SB).

The highest values of Zr/Nb ratio are considered to define the coarsest sediment (which could represent a SB), while the lowest values correspond to an MFS.

Figure 11 shows that around the C2-1/C2-2 chemo subzones boundary, Zr/Nb ratio displays an SB limit.

Just above the S1A paly-subzone the interval presents a decreasing Zr/Nb sequence with negative trend that could be interpreted as a separate sequence characterizing fining upward sequence or transgressive sequence. However, the D4A and D3 paly zone/subzone are marked by an
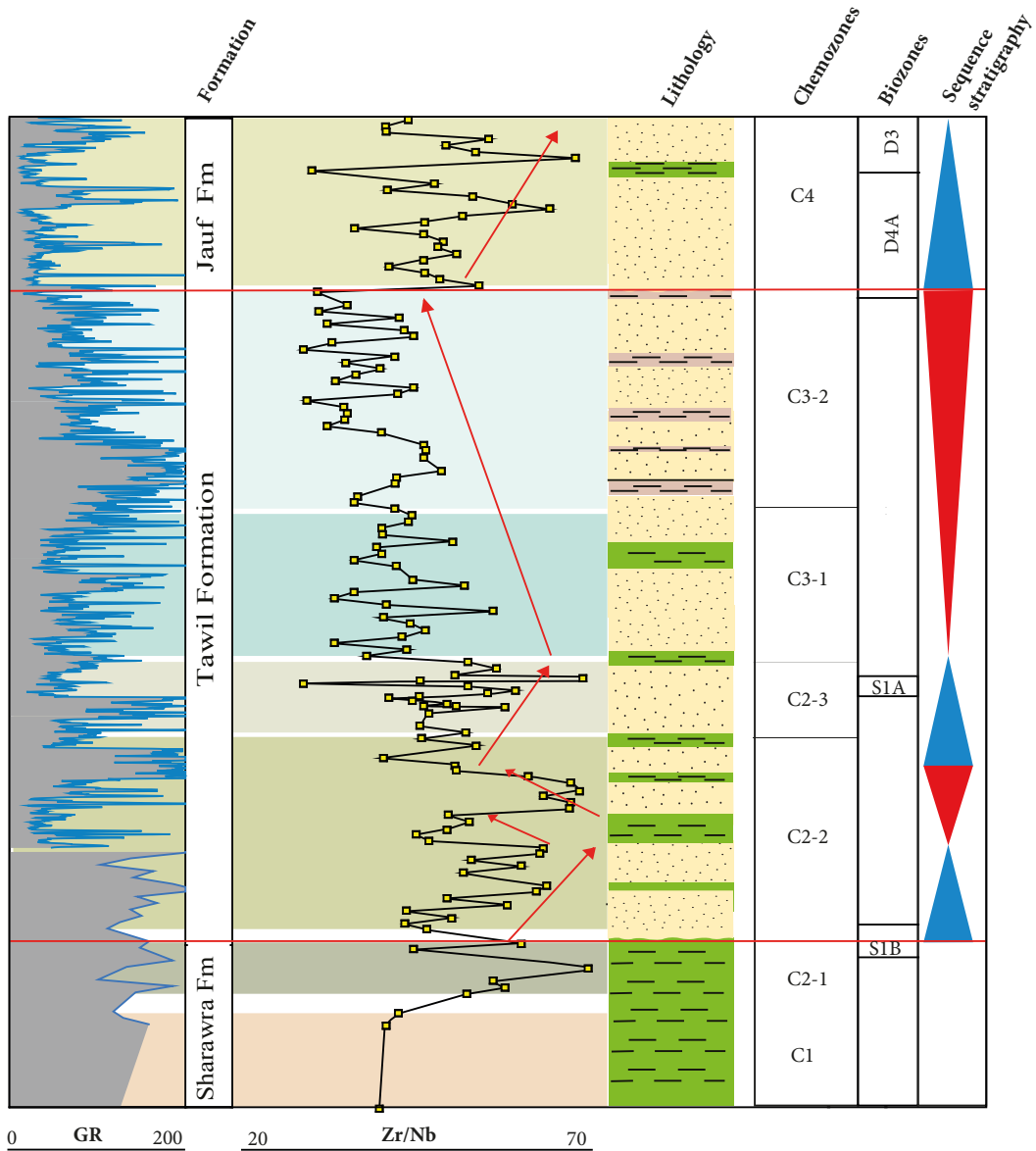

Figure 11. Zr/Nb ratio variation within the generated Chemo zones and related subzones (well-15-252) and its interpretation in terms of sequence stratigraphy.

increasing Zr/Nb interval with positive trend in the lower part, which could be interpreted as regressive sequence.

This holds true also for the sedimentological interpretation made by Dossary et al. (2017) on the same area of study.

4. Conclusion

In this study, a series of chemozones have been defined in the Tawil Formation, which lies between the upper Sharawra and the lower Jauf formations bounding. The scheme shows considerable potential for high-resolution correlation in the subsurface. The elemental abundances and ratios used to define the chemostratigraphic correlation schemes and chemostratigraphic boundaries in this study include Zr/Nb, (Zr*Hf)/(Nb*Ta), (Zr*Hf)/Nb, and Zr/(Nb*Ta). They reflect changes in sediment provenance and source area. These variations led to the differentiation of a hierarchical order of four chemozones and five subzones. The key element ratios used for chemostratigraphic purposes were, Zr/Nb, Nb/U, (Rb+Cs)/La, Al/(Ca+Mg+K+Na), (Zr*Hf)/(Nb*Ta), (Zr*Hf)/Nb, and Zr/(Nb*Ta); the zonal ratio characteristics are:

Zones C1 and C3 are characterized by the lowest values of Zr/Nb and (Zr*Hf)/(Nb*Ta), compared to the intervening Zone C2 and Zone C4.

Of the three C2 subzones, C2-2 produces lower values of Zr/(Nb*Ta) than the underlying C2-1 and overlying C2-3 subzones. Subzones C2-1, C2-2 and C2-3 have been recognized in Wells 15-252 and 608-215, with subzone C2-1 is being absent in the latter well.

Two subzones are associated with Zone C3 (C3-1 and C3-2), their differentiation is based on variation in the (Zr*Hf)/Nb ratio. Subzones C3-1 and C3-2 have been recognized in Wells 15-252, 608-1009, and 608-215. Definition of these subzones are based on the elements Zr, Hf, Nb, and Ta. In general, Zr and Hf are concentrated in zircon; Nb and Ta are associated with Nb-bearing and Ta-bearing heavy minerals, respectively. This ratio is entirely related to changes in provenance/source area.

The stratigraphic subzones identified from this chemostratigraphic study show, in some wells, good agreement with the recognized lithostratigraphic and biostratigraphic schemes, but this is not always the case. Zone C1 is generally associated with the Sharawra Formation, Zones C2 and C3, with the Tawil Formation, and Zone C4 broadly defines the Jauf Formation. Therefore, the chemostratigraphic zonal boundaries do not precisely correspond to biostratigraphical and formational boundaries, indicating that the C1-C2 and C3-C4 boundaries are probably time-transgressive. For example in Well-608-1009, Zone C1 defines most of the Tawil Formation, while in Well-608-465 Zone C2 is likely to be associated with both the upper part of the Sharawra and the Tawil formations. This suggests that the aforementioned lithostratigraphic units were probably deposited in multiple fluvio-deltaic systems, fed by sediments from the same clastic sources, active at different periods of time. This is in accordance with the published sedimentological interpretation conducted on the same wells, which confirms that the environment of deposition is mostly represented by fluvial distributary channels tidally influenced within an overall deltaic setting.

In order to model sequence stratigraphy, Zr/Nb ratio was used. It is considered as a proxy for grain size. Generally, Zr is associated with zircon heavy mineral and Nb is concentrated with Nb-bearing heavy minerals and clay minerals such as illite. The increasing Zr/Nb ratio values are considered to define the coarsening upward or regressive sequences while decreasing Zr/Nb trends can mark fining upward or transgressive sequences. These results comply very well with those of the previous studies.

References

Al-Hajri S, Filatoff J, Wender LE, Norton AK (1999). Stratigraphy and operational palynology of the Devonian System in Saudi Arabia. GeoArabia 4 (1): 53-68.

Al-Hajri S, Owens B (2000). Sub-surface palynostratigraphy of the Palaeozoic of Saudi Arabia. Stratigraphic Palynology of the Palaeozoic of Saudi Arabia. GeoArabia Special Publication 1: 10-17.

Al-Hajri S, Paris F (1998). Age and palaeoenvironment of the Sharawra Member (Silurian of North-Western Saudi Arabia). Geobios 31 (1): 3-12.

Al-Ramadan KA, Hussain M, Imam B, Saner S (2004). Lithologic characteristics and diagenesis of the Devonian Jauf sandstone at Ghawar Field, eastern Saudi Arabia. Marine and Petroleum Geology 21 (10): 1221-1234.

Armstrong HA, Turner BR, Makhlouf IA, Williams M, Al Smadi A, Abu Salah A (2005). Origin sequence stratigraphy and depositional environment of an Upper Ordovician Hirnantian) peri-glacial black shale, Jordan: Palaeogeography, Palaeoclimatology, Palaeoecology 220: 273-289.

Bigot M (1970). Geology of the Tabuk and Jauf Formations in the Wadi Al-Fajr area," BRGM, 70 Jed 28, Directorate General of Mineral Resources, Ministry of Petroleum and Mineral Resources

Cocker JD, Knox WO'B, Lott GK, Milodowski AE (2003). Petrologic controls on reservoir quality in the Devonian Jauf Formation sandstones of Saudi Arabia. GeoFrontier (1) : 6-11.

Dossary N, Tourqui H, Breuer P, Soua M, Lacsamana E (2017). Tawil Formation, Eastern Saudi Arabia: Sequence Stratigraphic Analysis and Implications for Better Understanding of Reservoir Heterogeneities. Middle East Region, Geosciences Technology Workshop, Amman, Jordan, May 15-16, 2017

Ellis DV (1987). Nuclear Logging Techniques (1987 PEH Chapter 50). Petroleum Engineering Handbook.

Ellwood BB, Tomkin JH, Ratcliffe KT, Wright AM, Kafafy AM (2008). Magnetic Susceptibility and Geochemistry for the Cenomanian/Turonian Boundary GSSP with Correlation to Time Equivalent Core. Palaeogeography, Palaeoclimatology, Palaeoecology 251 (1): 1-22.

Fralick PW, Kronberg BI (1997). Geochemical discrimination of clastic sedimentary rock sources. Sedimentary Geology 113 (1): 111-124.

Fujimaki H (1986). Partition coefficients of Hf, Zr, and REE between zircon, apatite, and liquid. Contributions to Mineralogy and Petrology 94 (1): 42-45.

Green TH, Pearson NJ (1983). Effect of pressure on rare earth element partition coefficients in common magmas. Nature 305 (5933): 414-416

Helal AH (1965). On the occurrence and stratigraphic position of Permo-Carboniferous illites in Saudi Arabia: Geologische Rundschau 54: 193-207.

Janjou D, Halawani M, Al-Muallem, MS, Robelin C, Brosse JM et al. (1997). Explanatory notes to the geological map of the Al Qalibah Quadrangle, Kingdom of Saudi Arabia. GeoscienceMap G-135, scale 1:250,000, sheet 28C. Deputy Ministry for Mineral Resources, Ministry of Petroleum and Mineral Resources, Kingdom of Saudi Arabia.

Laboun AA (2010). Paleozoic tectono-stratigraphic framework of the Arabian Peninsula. Journal of King Saud University-Science 22 (1): 41-50.

Mahmoud MD, Vaslet D, Husseini, MI (1992). The Lower Silurian Qalibah Formation of Saudi Arabia: An Important Hydrocarbon Source Rock (1). AAPG Bulletin 76 (10): 1491-1506.

Mange MA, Morton AC (2007). Geochemistry of heavy minerals. In: Mange MA, and Wright DT (editors). Heavy Minerals in Use. Developments in Sedimentology 58: 345-391.

McLennan SM (1989). Rare earth elements in sedimentary rocks; influence of provenance and sedimentary processes. Reviews in Mineralogy and Geochemistry 21 (1): 169-200.

Morton AC, Hallsworth C (1994). Identifying provenance-specific features of detrital heavy mineral assemblages in sandstones. Sedimentary Geology 90 (3): 241-256.

Pearce TJ, Besley BM, Wray DS, Wright DK (1999). Chemostratigraphy: a method to improve interwell correlation in barren sequences- a case study using onshore Duckmantian/Stephanian sequences (West Midlands, U.K.). Sedimentary Geology 124: 197-220.

Pearce TJ, Wray DS, Ratcliffe KT, Wright DK, Moscariello A (2005). Chemostratigraphy of the Upper Carboniferous Schooner Formation, southern North Sea. In: Carboniferous hydrocarbon geology: the southern North Sea and surrounding onshore areas. In: Collinson, J.D., D.J., Evans, D.W. Holliday, and N.S. Jones (eds.) Yorkshire Geological Society, Occasional Publications series (7): 147-164.

Pettijohn FJ, Potter PE, Siever R (1987). Sand and sandstone. Springer Science & Business Media.

Powers RW, Ramirez LF, Redmond CD, Elberg EL (1966). Geology of the Arabian Peninsula. Sedimentary geology of Saudi Arabia: U. S. Geological Survey Professional Paper 560-D.

Powers RW (1968). Lexique stratigraphique international. Volume III, Asie, Fas. 10b1, Arabia Saoudite. Centre Nationale de la Recherche Scientifique, Paris, France.

Rahmani RA, Steel RJ, Duaiji AA (2002). Concepts and methods of high-resolution sequence stratigraphy: Application to the Jauf gas reservoir, Greater Ghawar, Saudi Arabia. GeoFrontier 1: 15-21.

Ratcliffe KT, Hughes AD, Lawton DE, Wray DS, F Bessa et al. (2006). A regional chemostratigraphically-defined correlation framework for the late Triassic TAG-I in Blocks 402 and 405a, Algeria. Petroleum Geoscience 12: 3-12.

Ratcliffe, KT, Morton A, Ritcey D, Evenchick CE (2008). Whole rock geochemistry and heavy mineral analysis as exploration tools in the Bowser and Sustut Basins, British Colombia, Canada. Bulletin of Canadian Petroleum Geology 55 (4): 320-336.

Ratcliffe, KT, Wright AM, Montgomery P, Palfrey A, Vonk A et al. (2010). Application of chemostratigraphy to the Mungaroo Formation, the Gorgon field, offshore Northwest Australia: Australian Petroleum Production and Exploration Association, Journal, 50th Anniversary Issue, 371-388.

Riboulleau, A, Bout-Roumazeilles V, Tribovillard N, Guillot F, Recourt P (2014). Testing provenance diagrams: lessons from the well-constrained Cariaco Basin. Chemical Geology 389: 91-103.

Sano JL, Ratcliffe KT, Spain DR (2013). Chemostratigraphy of the Haynesville Shale. In: Hammes U, Gale L (editors). Geology of the Haynesville Gas Shale in East Texas and West Louisiana, USA. AAPG Memoir 105: 137-154.

Schock HH (1979). Distribution of rare-earth and other trace elements in magnetites. Chemical Geology 26 (1-2): 119-133

Serra O, Baldwin J, Quirein J (1980). Theory, interpretation, and practical applications of natural gamma ray spectroscopy. In: SPWLA 21st Annual Logging Symposium.

Sharland PR, Archer R, Casey DM, Davies RB, Hall SH et al. (2001). Arabian Plate Sequence Stratigraphy. GeoArabia Special Publication 2, Gulf PetroLink, Bahrain.

Shaw PJA (2003). Multivariate Statistics for the Environmental Sciences, London, UK: Hodder Arnold.

Soua M (2014). Paleozoic oil/gas shale reservoirs in southern Tunisia: An overview. Journal of African Earth Sciences (100): 450-492.

Soua M (2016). Chemostratigraphic approach: a tool to unravel the stratigraphy of the Permo-Carboniferous Unayzah Group and Basal Khuff Clastics Member, Central Saudi Arabia, Fall 2016 Saudi Aramco Journal of Technology 88-103.

Steemans P, Wellman CH, Filatoff J (2007). Palaeophytogeographical and palaeoecological implications of a miospore assemblage of earliest Devonian (Lochkovian) age from Saudi Arabia. Palaeogeography, Palaeoclimatology, Palaeoecology 250 (1): 237-254.

Steineke M, Bramkamp RA, Sander NJ (1958). Stratigraphic relations of Arabian Jurassic oil. In: Weeks LG (editor). Habitat of Oil: American Association of Petroleum Geologists 1294-1239

Stump TE, Al-Hajri S, Van der Eem JGLA (1995). Geology and biostratigraphy of the Late Precambrian through Palaeozoic sediments of Saudi Arabia. Review of Palaeobotany and Palynology 89 (1): 5-17.

Svendsen J, Friis H, Stollhofen H, Hartley N (2007). Facies discrimination in a mixed fluvio-eolian setting using elemental whole-rock geochemistry—applications for reservoir characterisation: Journal of Sedimentary Research 77: 23-33.

Wallace CA, Dini SM, Al-Farasani AA (1996). Explanatory notes to the geological map of the Ash Shuwahitiya Quadrangle, Kingdom of Saudi Arabia. Geoscience Map GM-125C, scale 1:250,000, sheet 30D. Deputy Ministry for Mineral Resources, Ministry of Petroleum and Mineral Resources, Kingdom of Saudi Arabia.

Wender LE, Bryant JW, Dickens MF, Neville AS, Al-Moqbel MA (1998). Paleozoic (pre-Khuff) hydrocarbon geology of the Ghawar area, eastern Saudi Arabia. GeoArabia 3 (2): 273-302.

Annex 1.1 – Major oxides (%), trace elements and rare earth elements (REE) concentrations (ppm) of well 15_252. Data is provided for min, max, and average values of each identified chemozones (C1 to C4). LREE: light rare earth elements; MREE: middle rare earth elements, and HREE: heavy rare earth elements.

Well	15_252											
Depth	Min	Max	Mean	Min	Max	Mean	Min	Max	Mean	Min	Max	Mean
Chemozone	C4			C3			C2			C1		
Al2O3	1.31	7.51	4.46	1.18	7.65	3.77	0.72	8.48	3.95	5.70	7.38	6.79
SiO2	68.28	94.07	78.63	77.46	91.15	85.40	67.92	94.63	86.25	74.21	79.37	76.16
TiO2	0.07	0.49	0.27	0.17	0.67	0.40	0.18	2.04	0.54	0.42	0.50	0.45
Fe2O3	1.00	6.88	2.67	0.42	2.65	1.43	0.37	9.76	1.91	1.43	2.55	2.06
MnO	0.03	0.63	0.18	0.00	0.02	0.01	0.00	0.77	0.06	0.04	0.11	0.06
MgO	0.21	1.97	0.83	0.07	0.70	0.21	0.06	1.69	0.35	0.59	1.20	0.83
CaO	0.41	1.92	1.04	0.21	0.90	0.44	0.17	1.17	0.54	0.74	1.19	0.95
Na2O	0.08	0.22	0.14	0.05	0.34	0.14	0.05	0.24	0.09	0.14	0.16	0.15
K2O	0.46	3.38	1.77	0.25	2.55	1.00	0.14	3.52	1.08	2.79	3.40	3.09
P2O5	0.04	0.30	0.08	0.02	0.34	0.10	0.03	0.18	0.07	0.04	0.09	0.06
Ba	6040	32256	14381	926	15466	4867	105	8357	2093	1208	2802	1838
Be	0.51	3.01	1.36	0.39	2.28	0.82	0.31	2.52	0.77	0.57	1.11	0.82
Co	2.67	7.06	4.62	1.39	6.98	2.67	0.94	15.72	3.64	4.02	5.39	4.95
Cr	13.57	56.10	29.18	5.06	79.09	22.61	8.20	106.39	24.92	17.36	29.36	24.00
Cs	0.32	4.50	1.26	0.23	3.41	1.05	0.23	3.82	1.16	1.61	2.57	2.13
Cu	4.50	29.36	10.03	0.03	252.34	16.60	0.29	48.02	8.10	5.34	12.29	8.35
Ga	1.50	10.78	5.58	1.40	10.30	4.80	1.24	10.28	4.82	6.88	9.20	8.22
Hf	1.97	10.91	6.03	3.41	12.38	7.46	3.75	98.45	13.00	8.19	10.92	9.25
Mo	1.04	12.21	4.39	0.21	21.82	2.26	0.31	15.13	1.21	0.51	2.62	1.14
Nb	1.42	10.05	5.47	3.53	11.94	7.47	3.71	34.74	9.18	8.12	10.15	8.68
Ni	2.30	9.70	5.89	0.42	48.98	4.72	0.14	34.06	5.69	7.56	10.89	9.61
Pb	35.09	232.33	84.00	7.49	225.37	20.96	2.69	303.77	22.68	9.29	36.73	17.58
Rb	10.51	94.81	44.40	7.54	90.53	29.08	4.83	88.10	29.63	75.98	100.54	86.51
Sc	0.64	6.91	2.99	0.82	5.57	2.56	0.73	7.79	2.87	2.44	4.55	3.40
Sn	0.13	1.23	0.47	0.25	23.38	1.25	0.25	2.44	1.00	0.87	1.30	1.09
Sr	177	748	408	137	1018	337	96	720	230	188	344	270
Ta	0.13	0.81	0.44	0.28	1.14	0.64	0.28	3.27	0.76	0.66	0.83	0.72
Th	2.38	14.03	6.33	5.52	23.29	14.55	4.59	200.33	23.03	13.65	19.73	15.78
Tl	0.07	0.33	0.17	0.04	0.35	0.14	0.03	0.48	0.18	0.41	0.52	0.46
U	0.87	6.32	2.31	1.26	7.16	3.19	1.36	17.31	3.64	3.07	4.29	3.60
V	5.57	46.97	21.68	7.71	40.38	21.77	8.69	45.71	22.76	21.02	30.69	26.84
W	2.01	10.25	4.08	2.19	413.19	18.03	0.77	33.51	4.09	1.40	1.99	1.56
Y	2.67	54.72	12.25	4.93	35.14	14.55	5.17	238.95	27.26	16.45	21.81	18.91
Zn	115.74	542.66	310.90	27.78	294.32	96.24	10.62	145.80	42.99	36.39	55.43	43.16
Zr	78.46	450.30	243.45	132.40	514.17	302.08	153.50	861.15	468.26	338.56	420.44	364.15
LREE	30.18	123.29	69.62	59.46	216.37	117.99	62.51	266.72	162.13	111.14	155.80	125.90
MREE	2.73	12.68	6.95	4.03	29.94	9.68	5.09	39.16	14.21	9.29	11.74	10.52
HREE	1.65	21.32	5.37	2.32	14.14	6.56	2.79	84.77	11.34	7.29	9.40	8.28

Annex 1.2 – Average values of utilized elemental ratios to identify the different chemozones of well 15_252 (C1 to C4).

Well	Chemozone	Zr/Nb	Zr/(Nb*Ta)	Nb/U	(Zr*Hf)/(Nb*Ta)	(Zr*Hf)/Nb	Zr/(Nb*Ta)
15_252	C4	46.45	132.71	2.52	130.28	279.25	19.51
	C3	40.96	761.85	2.50	208.82	307.89	25.82
	C2	52.87	177.55	2.63	549.31	640.42	38.62
	C1	41.97	290.66	2.43	281.56	388.07	30.14

Annex 2.1 – Major oxides (%), trace elements and rare earth elements (REE) concentrations (ppm) of well 608_215. Data is provided for min, max and average values of each identified chemozones (C1 to C4).

Well	608_215											
Depth	Min	Max	Mean	Min	Max	Mean	Min	Max	Mean	Min	Max	Mean
Chemozone	C4			C3			C2			C1		
Al2O3	1.91	6.12	4.59	3.27	7.37	5.78	0.77	7.84	4.25	0.34	8.93	3.55
SiO2	73.30	91.70	82.23	85.44	89.69	87.44	69.77	97.86	89.49	79.49	98.28	90.17
TiO2	0.15	0.31	0.22	0.06	0.36	0.19	0.03	0.41	0.16	0.03	0.73	0.22
Fe2O3	1.03	2.08	1.46	1.00	1.94	1.30	0.07	12.30	1.65	0.05	2.01	0.51
MnO	0.13	0.34	0.22	0.10	0.27	0.20	0.00	1.81	0.20	0.00	0.07	0.01
MgO	0.19	0.52	0.37	0.32	0.61	0.42	0.08	1.87	0.36	0.07	0.87	0.27
CaO	0.28	0.40	0.36	0.30	0.47	0.37	0.15	0.53	0.33	0.17	1.18	0.48
Na2O	0.13	0.34	0.26	0.26	0.39	0.33	0.10	0.45	0.25	0.07	0.37	0.18
K2O	1.00	3.13	2.38	1.71	3.58	2.78	0.22	3.39	1.50	0.07	3.67	1.05
P2O5	0.02	0.07	0.04	0.01	0.03	0.02	0.01	0.04	0.02	0.01	0.23	0.03
Ba	207	582	406	493	749	593	145	11782	1651	182	7782	1491
Be	0.35	0.89	0.68	0.40	0.88	0.68	0.32	2.33	0.88	0.29	1.68	0.54
Co	3.26	11.00	7.03	1.58	5.42	3.36	1.27	8.70	2.41	1.12	8.56	2.42
Cr	8.92	13.74	10.58	5.10	16.60	10.08	3.81	17.65	10.83	5.21	42.48	14.45
Cs	0.81	3.68	2.40	1.40	3.71	2.81	0.40	5.12	2.44	0.24	3.04	1.13
Cu	4.52	10.87	7.09	1.80	6.50	4.73	0.55	33.58	6.34	0.24	10.90	2.39
Ga	2.00	7.35	5.14	3.31	7.41	5.89	0.91	8.32	4.56	0.57	11.44	4.15
Hf	4.21	9.27	6.04	1.87	7.57	4.03	0.89	11.68	4.24	0.87	31.11	7.57
Mo	0.62	1.23	0.87	0.24	2.40	1.11	0.41	1.05	0.67	0.42	1.14	0.72
Nb	3.03	5.90	4.14	1.19	6.55	3.72	0.58	8.14	3.32	0.72	13.66	4.27
Ni	3.22	8.25	5.78	2.03	8.48	3.85	0.05	7.62	2.05	0.06	12.98	2.96
Pb	43.30	62.20	55.05	14.08	28.97	23.00	5.39	31.66	20.53	2.71	326.32	23.42
Rb	19.88	84.22	58.19	37.04	81.05	64.29	6.05	82.63	39.51	2.41	94.52	24.58
Sc	1.38	1.74	1.60	0.84	1.99	1.46	0.31	4.34	1.54	0.26	4.38	1.69
Sn	0.84	0.89	0.87	0.65	1.37	1.04	0.32	2.25	0.98	0.27	2.16	0.81
Sr	42	178	128	95	160	127	46	233	111	44	992	173
Ta	0.24	0.49	0.34	0.09	0.50	0.30	0.07	0.65	0.28	0.07	1.21	0.36
Th	2.29	7.71	4.67	1.22	7.35	3.58	0.92	10.39	3.77	0.91	46.08	7.03
Tl	0.15	0.25	0.21	0.12	0.23	0.18	0.04	0.27	0.12	0.01	0.31	0.11
U	1.15	5.96	2.96	0.90	4.94	2.35	0.40	5.70	1.71	0.57	7.68	2.23
V	7.50	12.40	9.57	4.65	16.28	9.73	3.86	20.28	10.56	2.83	35.70	14.71
W	1.08	1.87	1.38	0.77	1.82	1.04	0.40	3.75	1.43	0.59	6.59	1.89
Y	13.76	22.24	18.51	5.24	11.65	9.22	5.25	22.50	10.77	5.57	53.41	15.34
Zn	525.94	6656.46	3081.67	143.93	547.36	302.33	19.21	367.61	95.42	19.24	97.13	42.64
Zr	174.14	333.81	231.14	62.25	306.37	159.47	33.76	458.95	167.53	31.19	1210.58	288.86
LREE	34.06	72.58	54.03	29.91	95.65	61.01	21.35	100.42	48.63	16.86	243.29	66.81
MREE	5.71	7.80	6.42	2.22	7.08	4.77	1.87	8.93	4.43	1.99	29.20	6.71
HREE	4.76	8.07	6.58	1.42	3.96	2.98	1.06	8.38	3.44	1.13	18.37	5.29

Annex 2.2 – Average values of utilized elemental ratios to identify the different chemozones of well 608_215 (C1 to C4).

Well	Chemozone	Zr/Nb	Zr/(Nb*Ta)	Nb/U	(Zr*Hf)/(Nb*Ta)	(Zr*Hf)/Nb	Zr/(Nb*Ta)
608_215	C4	55.66	116.80	2.30	127.51	337.32	18.76
	C3	43.43	137.10	2.09	61.38	177.56	12.94
	C2	49.19	119.77	2.13	101.25	220.33	14.39
	C1	64.74	203.92	1.81	367.20	540.80	24.53

Annex 3.1 – Major oxides (%), trace elements and rare earth elements (REE) concentrations (ppm) of well 608_465. Data is provided for min, max, and average values of each identified chemozones (C1 to C3).

Well	608_465								
Depth	Min	Max	Mean	Min	Max	Mean	Min	Max	Mean
Chemozone	C3			C2			C1		
Al2O3	1.17	2.52	1.98	1.17	7.50	3.23	2.92	7.10	5.48
SiO2	83.44	90.18	87.48	77.80	92.84	87.24	66.04	87.24	77.38
TiO2	0.16	0.52	0.33	0.17	0.78	0.41	0.32	0.53	0.41
Fe2O3	0.25	0.65	0.49	0.21	2.11	0.72	1.42	2.58	1.95
MnO	0.00	0.01	0.01	0.00	0.02	0.01	0.00	0.12	0.05
MgO	0.22	1.34	0.73	0.07	2.06	0.37	0.18	0.85	0.53
CaO	0.51	1.96	1.27	0.19	2.60	0.61	0.34	1.01	0.64
Na2O	0.10	0.24	0.14	0.08	0.22	0.12	0.13	0.31	0.19
K2O	0.39	0.77	0.58	0.42	1.45	0.69	1.17	3.25	2.40
P2O5	0.01	0.03	0.02	0.01	0.09	0.04	0.03	0.32	0.07
Ba	7766	26070	13466	3694	42734	9588	8737	93074	30965
Be	0.40	1.01	0.69	0.37	4.30	0.98	0.49	1.54	0.91
Co	1.61	2.65	1.98	1.35	8.93	2.00	1.96	8.00	4.75
Cr	7.18	24.40	17.13	12.35	55.12	23.25	14.92	94.02	36.11
Cs	0.40	2.04	0.95	0.33	1.96	0.68	0.64	3.21	1.87
Cu	2.68	24.99	8.51	0.67	18.70	2.61	2.72	24.00	11.42
Ga	1.67	3.52	2.87	1.62	9.44	4.30	3.45	9.53	6.52
Hf	3.19	10.01	6.69	2.88	18.74	9.06	6.11	16.48	9.94
Mo	0.85	3.22	2.00	0.56	4.31	1.39	0.61	18.37	3.97
Nb	2.92	8.83	5.88	2.80	11.13	7.07	6.56	11.20	8.32
Ni	0.03	4.55	1.91	0.22	77.75	5.94	0.89	47.53	12.53
Pb	28.10	50.81	37.16	17.08	132.82	39.97	32.83	204.28	67.23
Rb	7.72	19.56	14.05	8.30	29.08	14.14	25.22	86.58	58.98
Sc	1.09	2.29	1.74	0.96	5.14	2.49	1.70	4.87	3.06
Sn	0.42	1.13	0.70	0.49	1.29	0.82	0.52	1.25	0.89
Sr	98	261	143	69	358	154	125	284	198
Ta	0.26	0.79	0.53	0.26	0.97	0.59	0.52	0.98	0.69
Th	5.09	22.57	11.31	4.57	28.28	14.14	10.60	23.92	16.69
Tl	0.04	0.09	0.07	0.04	0.19	0.09	0.08	0.33	0.21
U	1.07	2.98	1.89	1.25	7.03	3.01	2.59	5.86	3.28
V	8.87	16.68	13.48	9.05	36.81	19.82	16.89	35.04	24.87
W	2.45	8.72	5.43	1.62	212.58	10.95	2.71	134.22	19.00
Y	5.21	10.17	8.65	6.73	47.14	14.40	12.98	27.37	19.77
Zn	41.11	93.53	58.59	24.54	143.02	58.51	44.91	118.66	76.38
Zr	121.15	431.14	274.40	113.53	788.81	374.81	227.27	624.35	368.03
LREE	48.86	112.42	73.98	59.52	229.01	124.43	97.56	209.79	130.03
MREE	3.63	7.31	4.87	4.53	26.53	9.44	9.20	15.21	11.76
HREE	2.20	5.00	3.88	3.01	16.07	6.19	5.66	10.37	7.96

Annex 3.2 – Average values of utilized elemental ratios to identify the different chemozones of well 608_465 (C1 to C3).

Well	Chemozone	Zr/Nb	Zr/(Nb*Ta)	Nb/U	(Zr*Hf)/(Nb*Ta)	(Zr*Hf)/Nb	Zr/(Nb*Ta)
608_465	C3	46.16	39.53	3.17	180.09	316.48	24.67
	C2	53.61	174.93	2.55	311.48	496.59	31.56
	C1	43.98	181.19	2.61	323.37	453.25	30.48

Annex 4.1 – Major oxides (%), trace elements and rare earth elements (REE) concentrations (ppm) of well 608_1003. Data is provided for min, max, and average values of each identified chemozones (C1 to C3).

Well	608_1003								
Depth	Min	Max	Mean	Min	Max	Mean	Min	Max	Mean
Chemozone	C3			C2			C1		
Al2O3	0.32	5.87	2.55	0.27	6.28	1.59	1.51	7.27	4.31
SiO2	46.02	96.88	84.13	78.19	98.71	93.51	44.06	90.29	70.08
TiO2	0.07	0.70	0.25	0.04	8.38	0.48	0.22	0.58	0.40
Fe2O3	0.05	6.01	0.93	0.03	5.04	0.26	0.45	5.34	2.97
MnO	0.00	0.30	0.05	0.00	0.32	0.01	0.00	0.58	0.15
MgO	0.02	2.97	0.42	0.04	0.52	0.17	0.20	4.38	1.48
CaO	0.10	6.28	0.97	0.12	0.95	0.31	0.23	5.52	2.04
Na2O	0.04	0.60	0.14	0.05	0.25	0.12	0.10	0.49	0.24
K2O	0.05	1.13	0.40	0.08	1.44	0.36	0.41	1.28	0.87
P2O5	0.01	0.06	0.02	0.01	0.10	0.02	0.04	0.08	0.06
Ba	36	79642	10743	18	4304	661	109	88459	23604
Be	0.17	1.25	0.48	0.14	1.06	0.38	0.49	1.56	1.07
Co	0.01	9.69	1.45	0.01	14.02	1.15	1.19	6.85	4.45
Cr	2.45	59.13	13.78	2.67	55.56	8.49	9.21	102.22	45.47
Cs	0.13	1.22	0.63	0.17	2.31	0.62	0.64	1.82	1.26
Cu	1.58	64.86	12.59	0.05	146.48	8.15	0.29	223.39	80.12
Ga	0.72	6.96	3.66	0.64	7.61	2.31	2.44	8.85	5.84
Hf	1.77	15.44	5.23	1.33	235.83	12.39	2.75	12.38	6.36
Mo	0.12	11.20	1.45	0.02	1.04	0.30	0.09	46.50	15.76
Nb	1.50	12.37	4.68	0.83	124.67	7.87	4.12	10.27	7.17
Ni	0.00	18.33	3.36	0.05	14.81	2.27	4.87	16.80	12.14
Pb	6.62	794.63	101.37	3.48	39.92	11.20	15.57	472.98	169.95
Rb	1.54	21.45	9.31	1.65	45.50	9.02	9.49	27.85	19.85
Sc	0.63	3.60	1.68	0.28	18.89	1.76	1.00	5.52	3.14
Sn	0.41	10.03	1.75	0.41	4.71	0.88	0.74	4.58	2.11
Sr	41	939	194	25	350	110	181	1220	472
Ta	0.15	1.01	0.41	0.08	10.48	0.66	0.35	0.82	0.57
Th	4.24	26.32	11.07	1.82	334.36	19.44	5.86	19.35	11.28
Tl	0.04	2.27	0.30	0.01	0.29	0.06	0.08	1.18	0.59
U	0.49	3.74	1.21	0.32	25.36	1.70	0.92	3.39	2.38
V	4.02	54.46	16.66	3.51	107.74	13.85	12.01	62.03	38.53
W	0.58	21.52	3.65	0.40	9.23	1.01	0.70	26.30	7.58
Y	3.79	16.81	8.83	2.09	71.60	11.61	6.69	19.87	13.41
Zn	7.03	788.64	120.20	5.79	27.98	14.23	17.00	4245.54	1289.34
Zr	64.74	585.44	201.52	49.90	9683.41	511.98	108.15	516.77	265.98
LREE	47.23	185.17	88.02	17.75	425.11	85.69	85.61	187.22	132.92
MREE	2.15	13.76	4.70	0.90	22.22	5.34	6.71	12.14	9.77
HREE	1.66	7.93	3.80	0.84	42.11	5.30	3.19	8.67	5.73

Annex 4.2 – Average values of utilized elemental ratios to identify the different chemozones of well 608_1003 (C1 to C3).

Well	Chemozone	Zr/Nb	Zr/(Nb*Ta)	Nb/U	(Zr*Hf)/(Nb*Ta)	(Zr*Hf)/Nb	Zr/(Nb*Ta)
	C3	42.19	33.37	4.32	141.44	237.51	17.64
608_1003	C2	55.76	723.02	4.34	5063.11	847.94	43.01
	C1	35.60	321.27	3.56	163.22	254.74	21.22

Annex 5.1 – Major oxides (%), trace elements and rare earth elements (REE) concentrations (ppm) of well 608_1009. Data is provided for min, max, and average values of each identified chemozones (C1 to C4).

Well	608_1009											
Depth	Min	Max	Mean	Min	Max	Mean	Min	Max	Mean	Min	Max	Mean
Chemozone	C4			C3			C2			C1		
Al2O3	0.38	7.11	2.65	0.62	12.36	3.04	0.80	6.09	2.66	1.13	15.34	3.48
SiO2	77.88	95.49	88.19	72.24	92.85	84.90	81.53	94.08	88.64	43.86	90.75	75.89
TiO2	0.01	1.05	0.17	0.04	3.88	0.53	0.10	1.75	0.50	0.13	0.81	0.29
Fe2O3	0.08	3.24	1.07	0.14	12.66	1.78	0.21	2.46	0.60	0.47	2.78	1.48
MnO	0.00	0.30	0.04	0.00	0.36	0.04	0.00	0.00	0.00	0.00	0.07	0.02
MgO	0.06	0.58	0.20	0.06	0.28	0.14	0.06	0.20	0.09	0.07	1.54	0.72
CaO	0.11	0.95	0.37	0.19	0.78	0.46	0.33	1.24	0.74	0.78	3.85	2.04
Na2O	0.06	0.39	0.18	0.14	0.26	0.20	0.08	0.29	0.18	0.11	0.52	0.22
K2O	0.13	3.02	0.89	0.17	3.95	1.01	0.26	1.58	0.80	0.32	1.41	0.69
P2O5	0.00	0.12	0.02	0.01	0.04	0.02	0.01	0.10	0.03	0.01	0.14	0.05
Ba	23	47381	1343	31	2541	488	191	2870	799	130	165577	27769
Be	0.31	3.91	0.90	0.27	2.14	0.61	0.34	1.32	0.61	0.41	3.76	0.97
Co	1.10	6.53	2.57	1.21	18.56	2.85	0.15	1.71	0.56	0.36	3.59	1.59
Cr	2.88	32.54	9.87	4.56	52.34	14.33	4.77	58.83	16.74	5.44	169.58	54.05
Cs	0.20	2.70	0.70	0.31	4.36	0.87	0.23	1.72	0.72	0.42	5.59	0.99
Cu	0.10	162.92	28.64	2.38	11.74	4.63	0.10	7.83	2.10	2.74	37.19	13.77
Ga	0.57	10.15	3.16	1.00	15.36	3.62	0.99	7.32	3.38	1.64	18.69	4.61
Hf	0.68	37.65	5.53	1.23	74.62	10.16	2.18	62.04	14.28	1.73	11.27	4.44
Mo	0.29	1.14	0.59	0.39	1.83	0.74	0.03	0.59	0.34	0.25	11.78	4.97
Nb	0.27	16.80	3.09	1.47	66.20	9.46	1.81	23.81	7.74	2.54	16.20	5.70
Ni	0.03	9.47	1.86	0.09	10.38	2.96	0.02	6.11	1.96	1.57	11.53	5.13
Pb	0.98	492.39	26.77	2.44	7.51	4.12	3.92	21.93	8.06	5.51	134.85	46.73
Rb	3.09	73.63	21.98	5.01	99.48	22.33	4.96	38.44	17.79	7.78	62.08	18.41
Sc	0.15	4.41	1.13	0.37	5.30	1.74	0.55	6.12	1.89	0.76	12.72	2.57
Sn	0.04	34.63	5.03	0.23	2.72	0.75	0.24	1.50	0.69	0.20	2.20	0.66
Sr	20	836	102	43	178	101	51	350	144	65	893	301
Ta	0.05	1.49	0.26	0.09	5.61	0.79	0.14	1.81	0.59	0.20	1.56	0.45
Th	0.83	19.46	3.35	2.07	120.63	15.22	1.66	52.22	11.38	3.49	33.67	8.55
Tl	0.02	0.44	0.08	0.02	0.62	0.09	0.02	0.20	0.07	0.04	1.52	0.58
U	0.40	9.50	1.43	1.51	14.02	4.06	1.35	9.66	4.09	1.25	7.55	2.69
V	2.38	37.94	10.88	6.24	101.90	24.38	6.38	63.69	18.32	11.25	66.34	24.90
W	0.03	8.53	0.94	0.49	2.95	0.95	0.65	1.89	1.04	0.76	7.40	2.31
Y	2.78	28.86	7.70	4.28	41.71	10.57	1.97	32.91	9.59	2.05	27.99	8.50
Zn	10.89	699.20	45.01	14.60	28.32	21.62	5.92	46.67	15.98	11.63	2253.66	710.79
Zr	22.04	1450.09	217.85	37.24	3215.30	429.75	77.47	2844.30	612.95	62.83	478.09	179.12
LREE	15.74	212.37	47.07	18.49	128.01	60.78	18.13	416.79	95.75	29.45	198.19	80.82
MREE	1.75	24.19	4.29	1.76	9.85	4.66	1.24	21.19	5.67	1.56	18.64	7.12
HREE	0.84	12.24	2.90	1.12	19.20	4.11	1.35	15.37	4.83	1.44	13.54	4.56

Annex 5.2 – Average values of utilized elemental ratios to identify the different chemozones of well 608_1009 (C1 to C4).

Well	Chemozone	Zr/Nb	Zr/(Nb*Ta)	Nb/U	(Zr*Hf)/(Nb*Ta)	(Zr*Hf)/Nb	Zr/(Nb*Ta)
608_1009	C4	68.76	65.31	2.21	196.97	408.29	18.24
	C3	42.03	122.60	1.84	1702.56	468.43	35.97
	C2	61.67	460.82	1.84	1671.91	1243.44	46.72
	C1	31.58	43.34	2.09	81.58	147.08	14.01